J. Fluid Mech. (1984), vol. 146, pp. 65–113
Printed in Great Britain

# Simulation of Taylor–Couette flow. Part 2. Numerical results for wavy-vortex flow with one travelling wave

By PHILIP S. MARCUS

Division of Applied Sciences and Department of Astronomy, Harvard University

(Received 26 July 1983 and in revised form 23 March 1984)

We use a numerical method that was described in Part 1 (Marcus 1984*a*) to solve the time-dependent Navier–Stokes equation and boundary conditions that govern Taylor–Couette flow. We compute several stable axisymmetric Taylor-vortex equilibria and several stable non-axisymmetric wavy-vortex flows that correspond to one travelling wave. For each flow we compute the energy, angular momentum, torque, wave speed, energy dissipation rate, enstrophy, and energy and enstrophy spectra. We also plot several 2-dimensional projections of the velocity field. Using the results of the numerical calculations, we conjecture that the travelling waves are a secondary instability caused by the strong radial motion in the outflow boundaries of the Taylor vortices and are not shear instabilities associated with inflection points of the azimuthal flow. We demonstrate numerically that, at the critical Reynolds number where Taylor-vortex flow becomes unstable to wavy-vortex flow, the speed of the travelling wave is equal to the azimuthal angular velocity of the fluid at the centre of the Taylor vortices. For Reynolds numbers larger than the critical value, the travelling waves have their maximum amplitude at the comoving surface, where the comoving surface is defined to be the surface of fluid that has the same azimuthal velocity as the velocity of the travelling wave. We propose a model that explains the numerically discovered fact that both Taylor-vortex flow and the one-travelling-wave flow have exponential energy spectra such that $\ln[E(k)] \propto k^1$, where $k$ is the Fourier harmonic number in the axial direction.

## 1. Introduction

In Part 1 (Marcus 1984*a*) we described a numerical method for calculating viscous flow between two rotating cylinders where the outer cylinder is held stationary and the inner cylinder rotates with angular velocity $\Omega_{\text{in}}$. In this paper we use the numerical method to compute several Taylor–Couette flows, and we describe and analyse the important physical properties of these flows. We consider only large-aspect-ratio flows where the height of the cylindrical Couette apparatus is much greater than the gap between the cylinders. An infinite aspect ratio allows us to treat the flow as periodic with fundamental wavelength $2\pi/\alpha$ in the axial, $z$, direction. The equations of motion that govern the fluid are the Navier–Stokes equation with no-slip boundary conditions at the cylinder walls and the kinematic condition that the velocity be divergence-free. Three independent dimensionless numbers appear in the Navier–Stokes equation: the radius ratio $\eta = a/b$ (where $a \equiv$ inner-cylinder radius, $b \equiv$ outer-cylinder radius), the dimensionless axial wavelength $\lambda = 2\pi/\alpha d$ (where $d = b-a$ is the gap width) and the Reynolds number $R = a\Omega_{\text{in}} d/\nu$ (where $\nu$ is the kinematic viscosity). Throughout this paper, unless otherwise specified, we use $d$ as the unit of length, $a\Omega_{\mathrm{in}}$ as the unit of velocity and $\rho d^3$ as the unit of mass, where $\rho$ is the fluid density.

### *Summary of low-Reynolds-number experiments with outer cylinder stationary*

It is well known that for each geometry, or $\eta$, and for each axial wavelength $\lambda$, there is a critical Reynolds number $R_{\mathrm{c}}(\eta)$ such that, for $R < R_{\mathrm{c}}(\eta)$ circular Couette flow,

$$v_\phi = \frac{\eta}{1-\eta^2}\left[\frac{1}{r}\left(\frac{1}{1-\eta}\right) - r(1-\eta)\right], \tag{1.1}$$

$$v_r = v_z = 0, \tag{1.2}$$

is a stable equilibrium. For $R > R_{\mathrm{c}}(\eta)$ circular Couette flow is unstable to axisymmetric 3-dimensional Taylor vortices. In the laboratory this flow appears as $N$ vortices with alternating circulation stacked vertically on top of each other. The early experimental study of Taylor–Couette flow was concerned with the precise determination of onset of the Taylor-vortex flow and the measurement of the torques produced by this flow.

At larger Reynolds numbers and $\eta \gtrsim \frac{1}{2}$ the Taylor-vortex flow is itself unstable to a non-axisymmetric wave travelling at an angular speed $s_1$. This wavy-vortex flow and its stability properties was first studied systematically by Coles in his classic 1965 paper. When the travelling wave is viewed in the proper rotating frame, this flow appears as a steady state with azimuthal wavelength $2\pi/m_1$, where $m_1$ is an integer usually less than 12 for $\eta \leqslant 0.9$. At still-larger Reynolds numbers, a second travelling wave appears (Shaw *et al.* 1982) with a second wave speed of $s_2$ and with wavenumber $m_2$ not necessarily equal to $m_1$. In the laboratory (inertial) frame this modulated wavy-vortex flow is quasi-periodic in time, but in the proper rotating frame it is periodic. At even larger Reynolds numbers with $\eta \approx 0.875$ these travelling waves disappear and are replaced by other non-axisymmetric disturbances (Zhang & Swinney 1984). As the Reynolds number is increased still further, the flow becomes chaotic.

### *Description of wavy-vortex flow*

In this paper we are primarily concerned with Taylor-vortex flow and the wavy-vortex flow with one travelling wave. King & Swinney (1983) have experimentally mapped the stability boundaries of the one-travelling-wave flow with $m_1 = 6$ in the $(R, \lambda)$-plane. In particular, for fixed radius ratio $\eta = 0.875$ and for fixed $\lambda$, as the Reynolds number is increased above a critical value there is a transition from the $m_1 = 6$ travelling wave to the $m_1 = 4$ or $m_1 = 5$ (depending on $\lambda$) travelling wave. Similarly, for $\eta = 0.875$ there is another critical Reynolds number (which is also a function of $\lambda$ and $\eta$) below which the $m_1 = 6$ travelling wave is unstable and makes a transition to an $m_1 = 4$ travelling wave. For fixed Reynolds number, as $\lambda$ is changed (by adiabatically filling and draining the Couette apparatus while keeping the actual number $N$ of vertically stacked Taylor vortices constant), it is found that there are minimum ($\lambda_{\mathrm{min}}(R) \approx 2.0$) and maximum ($\lambda_{\mathrm{max}}(R) \approx 4.0$) values of $\lambda$ between which the $m_1 = 6$ wave is stable. If $\lambda$ is decreased below $\lambda_{\mathrm{min}}(R)$ the Taylor cells become too 'fat' in the radial direction and there is a transition in which the number of Taylor-vortex pairs decreases by one or two. This transition increases the value of $\lambda$ by a discrete amount. There is an analogous transition if $\lambda$ becomes too large and the Taylor vortices become too 'thin'.

Experiments show that the wave speeds of the travelling waves in wavy-vortex flow depend strongly on the geometry (King *et al.* 1984). The speeds are always a strong function of radius ratio $\eta$, but for large aspect ratio $\Gamma$ they are only weakly dependent on $\Gamma$. At low Reynolds number the wave speeds are sensitive to the values of $R$, $\lambda$ and $m_1$, but at high Reynolds number the speeds asymptotically approach a constant value that depends primarily on the radius ratio. It must be emphasized that, as Coles discovered for most given values of $R$, $\Gamma$ and $\eta$, there is not a unique stable flow; there is a discrete spectrum of allowable axial wavelengths $\lambda$ and azimuthal wavenumbers $m_1$ (and possibly $m_2$). We also remind the reader that, near the stability boundaries of a flow, more-exotic states are possible where several different travelling-wave flows coexist with each other (King 1983).

### *Purpose of paper*

At the present time it is analytically impossible to calculate non-axisymmetric equilibrium flows except for $R$ slightly greater than $R_c$; however, Stuart (1958), in a remarkable paper, used a finite-amplitude theory to find the dependence of torque on Reynolds number in axisymmetric Taylor vortex flow. Stuart's amplitude theory was improved upon by Davey (1962), who allowed the fundamental Taylor-vortex mode to generate harmonics. Davey, DiPrima & Stuart (1968) used amplitude calculations to predict the onset of 3-dimensional wavy-vortex flow and determine its torque. Eagles (1971) confirmed the findings of Davey *et al.* by a higher expansion. An excellent summary of these and other amplitudes calculations appears in the review article by DiPrima & Swinney (1981).

Well-resolved axisymmetric flows have been previously computed numerically by Meyer (1966) and more recently by Meyer-Spasche & Keller (1980). Three-dimensional linearized eigenfunctions and numerically truncated one-travelling-wave flows have been computed by Meyer (1969*a*, *b*), Jones (1981) and Yahata (1983, and his previous papers cited therein). Yahata's calculations are extremely under-resolved and show spurious temporal behaviour (see Part 1). A well-resolved calculation of 3-dimensional Taylor–Couette flow has been carried out by Moser, Moin & Leonard (1983).

The purpose of the present paper is to simulate non-axisymmetric time-dependent equilibrium flows and the transitions among them, using a numerical method that was developed and tested in Part 1 and compared with the laboratory data in King *et al.* (1984). In the latter paper we showed that we can calculate the speeds of the travelling wave to within their experimental uncertainty of 0.2 %. The numerical code allows us to compute accurate flows for Reynolds numbers up to approximately $15R_c$. Since all of the transitions and flows described in this section occur in this Reynolds-number regime, we have a useful tool for studying the physics of these nonlinear flows. By knowing the velocity field at every point, we can calculate the energies, angular momenta, torques, enstrophies, energy dissipation rates and wave speeds for several nonlinear flows. Although it is impracticable to sample numerically the $(R, \lambda, \eta, m_1)$ parameter space in as much detail as can be done experimentally, for a few flows we can get a numerical physical description that is far more detailed than is obtainable from current experiments.

Analytic finite-amplitude and linearized or truncated numerical studies have given us many mathematical details of wavy-vortex flow, and the experimental studies have supplied us with stability diagrams, wave-speed measurements and torque–Reynolds-number relations, but surprisingly little *physical* understanding of Taylor–Couette flow has been gained since Rayleigh (1920) explained the inviscid centrifugal instability that governs the formation of Taylor vortices. Several authors (Coles 1965; Meyer 1966; Davey *et al.* 1968; Jones 1981) have suggested possible scenarios by which the axisymmetric vortex flow becomes unstable to 3-dimensional waves, but no single picture of the 3-dimensional instability of Taylor-vortex flow has emerged that is as compelling as Rayleigh's explanation of the instability of circular Couette flow to Taylor vortices. It is also unfortunate that, except for Jones, few authors have tried to explain what determines the speed of the travelling waves.

In this paper we use a nonlinear numerical simulation to demonstrate how the speed of the non-axisymmetric travelling wave (at onset) is determined by the axisymmetric Taylor vortices. By computing the energy and enstrophy spectra, we show energy is transferred from the motor driving the inner cylinder to the mean axisymmetric swirl, to the Taylor-vortex flow, and then distributed among the modes that make up the wavy-vortex flow. Furthermore, by using the spatial symmetries of the flow, the computer-generated maps of the 3-dimensional velocity, and energy-transfer arguments, we propose a possible physical explanation for the instability that produces travelling waves.

In §2, we review the physics of Taylor-vortex flow and examine the spatial symmetries that are possible for Taylor-vortex flow and non-axisymmetric wavy-vortex flow. The results of our numerical simulation of Taylor-vortex flow are in §3. In §4 we present our results of the simulations of the one-travelling-wave flow at low Reynolds numbers. We determine the physical properties of the flow as functions of $m_1$, $\lambda$ and $R$ and present our conjecture that the travelling waves are a secondary instability caused by the radial jets between Taylor vortices. In §4 we also calculate the wave speeds and show how the wave speed is determined when the Reynolds number is equal to the critical value for the onset of wavy-vortex flow. Our discussion appears in §5. In the Appendix we use marginal stability theory and mixing-length theory for Taylor–Couette flow at large Reynolds number to derive the characteristic azimuthal, axial and radial velocities both within and far from the boundary layers.

## 2. Spatial symmetries of Taylor–Couette flow

Before presenting the results of our numerical calculations, we review the spatial symmetries of Taylor–Couette flow. Knowing what symmetries are allowed and disallowed makes the numerical calculation of the flow easier (see Part 1). Circular Couette flow (see (1.1) and (1.2)) is 2-dimensional; there is no axial component of the velocity nor is it a function of $z$. There are no other known 2-dimensional stable equilibrium Taylor–Couette flows, although *time-dependent* 2-dimensional Taylor columns have been observed (see e.g. figure 22*o* of Coles 1965). This lack of 2-dimensional equilibria is examined in a subsequent paper (Marcus 1984*b*), in which it is shown that enstrophy conservation inhibits 3-dimensional instabilities of circular Couette flow.

Although Taylor-vortex flow is 3-dimensional, it is axisymmetric. Since the vortex flow is driven by centrifugal instability it is not surprising that one of its characteristic features is the nonlinear advection of angular momentum from the inner cylinder to the outer cylinder. The mean radial component of the angular-momentum flux $F_L$ is (see Part 1)

$$F_L = \frac{1}{2\pi\lambda}\left[R^{-1}r^2\int \frac{\partial(v_\phi/r)}{\partial r}\,\mathrm{d}\phi\,\mathrm{d}z + r\int v_r\,v_\phi\,\mathrm{d}z\,\mathrm{d}\phi\right]. \tag{2.1}$$

For large-Reynolds-number flows the angular-momentum flux far from the boundaries is carried by the nonlinear term in (2.1). Consequently, $v_r$ and $v_\phi$ are well-correlated in Taylor-vortex flow. A schematic plot in the $(r,\phi)$-plane (for constant value of $z$) of an axisymmetric flow where $v_r$ and $v_\phi$ are well-correlated (i.e.

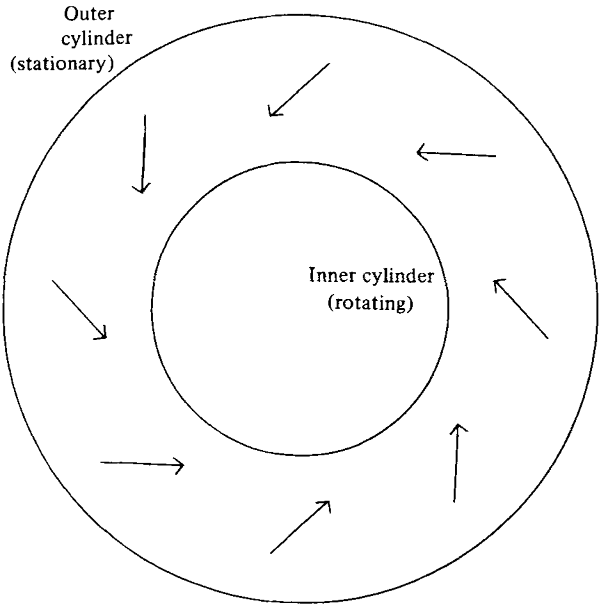

FIGURE 1. Schematic of the axisymmetric Taylor-vortex velocity projected onto the $(r, \phi)$-plane at $z = 0$. Taylor vortices transport angular momentum from the inner cylinder to the outer cylinder because $\int\int v_r v_\phi \, \mathrm{d}\phi \, \mathrm{d}z$ is non-zero.

$\int v_r v_\phi \, \mathrm{d}z \, \mathrm{d}\phi / (\int v_r^2 \, \mathrm{d}\phi \, \mathrm{d}z \int v_\phi^2 \, \mathrm{d}\phi \, \mathrm{d}z)^{\frac{1}{2}} \rightarrow 1)$ is shown in figure 1. To a first approximation, Taylor vortices look like that plot periodically repeated at the planes: $z = 0, \pm\lambda, \pm 2\lambda, \pm 3\lambda, \ldots$. Midway between these planes at $z = \pm\frac{1}{2}\lambda, \pm\frac{3}{2}\lambda, \pm\frac{5}{2}\lambda, \ldots$ the flow also looks like figure 1 with the arrows reversed but maintaining the same correlation and transporting angular momentum at the same rate. The velocity fields at $z = 0$ and $z = \frac{1}{2}\lambda$ are connected by a flow upward along the inner cylinder and downward along the outer cylinder so the flow is divergence-free. The net result is that Taylor vortices do not lie in the $(r, z)$-planes, but are twisted, and have some component in the $\hat{e}_\phi$-direction. If the vortices did not have this twist they could not transport angular momentum. Taylor-vortex flow is the sum of the azimuthal circular Couette flow plus the flow in the Taylor vortices. A fluid element follows a helical path where the central axis of the helix is wound around the inner cylinder. Although angular momentum is transported outward in this flow, the fluid near the axis of the helix (the centre of the Taylor vortices) does not mix at all with the fluid near the walls of the cylinders. The latter fluid mixes with the fluid in the inflow and outflow jets of the Taylor vortices (see §3). The lack of fluid mixing at the centres of the Taylor vortices has important physical consequences that are examined in §4.

### *Physical symmetries and Fourier coefficients*

Every physical symmetry of a flow corresponds to a relationship among the Fourier coefficients of the velocity field. Since our numerical method decomposes the velocity into Fourier sums in the axial and azimuthal directions, these symmetries are easy to detect and impose. For example, spirally symmetric flows, which look like barber poles, have Fourier representations of the form

$$v_r(r, \phi, z, t) = \sum_{m, k} \frac{2\pi k}{\lambda} f_{m,k}(r, t) \cos\left(m\phi + \frac{2\pi k z}{\lambda}\right), \tag{2.2}$$

$$v_\phi(r,\phi,z,t) = \sum_{m,k} \frac{2\pi k}{\lambda} g_{m,k}(r,t) \sin\left(m\phi + \frac{2\pi kz}{\lambda}\right), \tag{2.3}$$

$$v_z(r,\phi,z,t) = \sum_{m,k} -\left(\frac{\partial r f_{m,k}}{\partial r} + m g_{m,k}\right) \frac{1}{r} \sin\left(m\phi + \frac{2\pi kz}{\lambda}\right), \tag{2.4}$$

where $f_{m,k}$ and $g_{m,k}$ are real functions of $r$ and $t$, with $f_{m,k} = g_{m,k} = \partial f_{m,k}/\partial r = 0$ at the radial boundaries. The velocity defined by (2.2)–(2.4) obeys viscous no-slip boundary conditions and is divergence-free. However, it is immediately apparent that spiral flows of this form have $\int v_\phi v_r \, \mathrm{d}z \, \mathrm{d}\phi$ identically equal to zero, and therefore have no nonlinear contribution to the angular-momentum transport. We have examined spirally symmetric linear perturbations and found that they decay, as do several other classes of flow with symmetries that explicitly prohibit nonlinear transport of angular momentum.

One rather trivial symmetry allowed by the Navier–Stokes equation and no-slip boundary conditions is the invariance of the velocity field under rotation about the $z$-axis by $2\pi/p$ (i.e. $\boldsymbol{v}(r,\phi,z,t) = \boldsymbol{v}(r,\phi+2\pi/p,z,t)$). Another allowed symmetry, discussed by Richtmyer (1981), occurs when the flow is invariant under $z \rightarrow -z$ and $v_z \rightarrow -v_z$ (i.e. the flow is invariant when the Taylor–Couette apparatus is turned upside down). This symmetry does not allow non-axisymmetric waves on the inflow or outflow boundaries, and we know of no experimental observations of non-axisymmetric Taylor-vortex flows that possess this symmetry when the outer cylinder is held stationary. In addition to being $p$-fold symmetric in $\phi$, a velocity field can have the more subtle symmetry

$$v_r(r,\phi,z,t) = v_r(r,\phi+\pi/p,\,-z,t), \tag{2.5}$$

$$v_\phi(r,\phi,z,t) = v_\phi(r,\phi+\pi/p,\,-z,t), \tag{2.6}$$

$$v_z(r,\phi,z,t) = -v_z(r,\phi+\pi/p,\,-z,t). \tag{2.7}$$

We call flows that have the form (2.5)–(2.7) 'shift-and-reflect' symmetric. This symmetry is preserved under the nonlinear multiplication in the full Navier–Stokes equation. Therefore finite-amplitude velocities as well as linear perturbations can have this symmetry. Note that circular Couette flow is a trivial example of a velocity field that has shift-and-reflect symmetry. For a general *axisymmetric* flow, the shift-and-reflect symmetry reduces to the $z \rightarrow -z$, $v_z \rightarrow -v_z$ symmetry discussed by Richtmyer. The shift-and-reflect symmetries are important not only because they allow nonlinear contributions to the angular-momentum transport but also because the observed axisymmetric Taylor-vortex flow and the non-axisymmetric one-travelling-wave wavy-vortex flows have these symmetries.

The velocity field $\boldsymbol{v}(r,\phi,z,t)$ can be written as a spectral sum

$$\boldsymbol{v}(r,\phi,z,t) = \mathrm{Re}\left[\sum_{m=-\infty}^{\infty} \sum_{k=0}^{\infty} \hat{\boldsymbol{v}}(r,m,k,t)\, \mathrm{e}^{\mathrm{i}m\phi}\, \mathrm{e}^{\mathrm{i}2\pi kz/\lambda}\right], \tag{2.8}$$

where the Fourier coefficients $\hat{\boldsymbol{v}}(r,m,k,t)$ are complex. In terms of the Fourier coefficients, the shift-and-reflect symmetry of (2.5)–(2.7) is

$$\hat{v}_r(r,m,k,t) = (-1)^m \hat{v}_r^*(r,\,-m,k,t), \tag{2.9}$$

$$\hat{v}_\phi(r,m,k,t) = (-1)^m \hat{v}_\phi^*(r,\,-m,k,t), \tag{2.10}$$

$$\hat{v}_z(r,m,k,t) = -(-1)^m \hat{v}_z^*(r,\,-m,k,t). \tag{2.11}$$

For axisymmetric flows the symmetry reduces to $\mathrm{Im}\,[\hat{v}_r] = \mathrm{Im}\,[\hat{v}_\phi] = \mathrm{Re}\,[\hat{v}_z] = 0$. For axisymmetric flows with shift-and-reflect symmetry the spectral sum in (2.8) can be written

$$v_r(r,z,t) = \sum_{k=0}^{\infty} f_k(r,t)\cos\frac{2\pi kz}{\lambda}, \tag{2.12}$$

$$v_\phi(r,z,t) = \sum_{k=0}^{\infty} g_k(r,t)\cos\frac{2\pi kz}{\lambda}, \tag{2.13}$$

$$v_z(r,z,t) = \sum_{k=0}^{\infty} h_k(r,t)\sin\frac{2\pi kz}{\lambda}, \tag{2.14}$$

where $f_k$, $g_k$ and $h_k$ are real functions.

Note that in physical space the shift-and-reflect symmetry depends upon the choice of origin of $z$ and $\phi$. If the $z$-origin were shifted by $z_0$ (where $z_0$ is not a multiple of $\frac{1}{2}\lambda$) the physical symmetry of the flow would not disappear, but (2.5)–(2.7) and (2.9)–(2.11) would no longer be true, and the correct equations that describe the symmetry would be more complicated. To use (2.9)–(2.11) with a flow that has shift-and-reflect symmetry, we need to choose the correct origin of the coordinate system.

Most of our numerical calculations for the one-travelling-wave flows were done by using a sparse set of Fourier modes that forced the flow to be invariant under rotation about the $z$-axis by $2\pi/m_1$ and to have the shift-and-reflect symmetry. The resulting equilibrium flows were then tested for stability with respect to all modes, including modes with no symmetries. Occasionally, flows were calculated using all of the Fourier modes, and after the solution converged a numerical search was done to find a coordinate system with an origin such that the equilibrium flow had the shift-and-reflect symmetry of (2.9)–(2.11). For radius ratios between 0.8 and 0.9 and for Reynolds numbers less than approximately $10R_\mathrm{c}$ we found that, when perturbations without shift-and-reflect symmetry were introduced into the numerically calculated flows, the perturbations decayed quickly in a dynamical time. For Reynolds numbers greater than approximately $10R_\mathrm{c}$ the perturbations grew occasionally into a two-travelling-wave flow (which cannot have shift-and-reflect-symmetry for $m_1 \neq m_2$).

Other allowable symmetries in Taylor–Couette flows and their implications for non-axisymmetric flows with wavy inflow (outflow) boundaries and unperturbed or straight outflow (inflow) boundaries (cf. Andereck, Dickman & Swinney 1983) are discussed by Marcus (1984*b*).

## 3. Numerical simulation of axisymmetric Taylor-vortex flow

Using the initial-value code developed in Part 1, we have computed several axisymmetric Taylor-vortex flows with three types of initial conditions: circular Couette flow with infinitesimal perturbations (i.e. the round-off noise of the computer); circular Couette flow with one or more of its linearly unstable eigenmodes; and unstable non-axisymmetric wavy-vortex flows. Taylor-vortex flow is stable only in a small region of $(\eta, R, \lambda)$ parameter space. In this stable region we find that the final steady state is independent of the initial conditions.

### *Stable equilibrium with* $\eta = 0.875$, $R_\mathrm{c} = 118.16$, $\lambda = 2.50$, $R = 1.179R_\mathrm{c}$

Although we have computed several stable equilibrium Taylor-vortex flows, we will present detailed results for only one of our numerical simulations. The stable

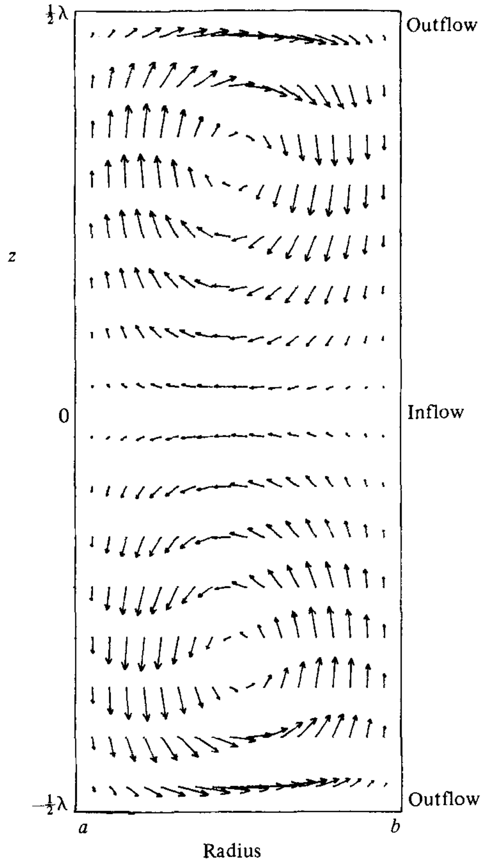

FIGURE 2. Two-dimensional projection of the Taylor-vortex velocity onto the $(r, z)$-plane with $\eta = 0.875$, $R = 1.179R_c$, $\lambda = 2.50$ and $R_c = 118.16$. The inner-cylinder boundary is on the left and the outer-cylinder boundary is on the right. The velocity field here and in all figures in §3 is computed with 33 radial Chebyshev polynomials and 32 axial Fourier modes.

Taylor-vortex flow with radius ratio $\eta = 0.875$, axial wavelength $\lambda = 2.50$ and Reynolds number $R = 139.32$ or $R = 1.179R_c$ typifies our results. In figure 2 we show a 2-dimensional projection of the velocity field in the radial–axial plane for some arbitrary (since the flow is axisymmetric) value of $\phi$. Here, as in all subsequent figures in the $(r, z)$-plane, the vertical line on the left side is the boundary of the inner cylinder, and the vertical line on the right is the outer cylinder. Note that the outflow boundary jet between the Taylor vortices at $z = \pm\frac{1}{2}\lambda$ has a much stronger shear velocity than the inflow boundary jet between the vortices at $z = 0$. The fact that the outflow boundary has a larger radial velocity has also been observed experimentally.

In figure 3 we have plotted the 2-dimensional projection of the velocity in the $(z, \phi)$-plane. In this figure, *as in all subsequent figures in the $(z, \phi)$-plane*, the vertical axis points in the axial direction and the horizontal axis points in the azimuthal direction. The velocity in figure 3 is the $(z, \phi)$-projection of $\boldsymbol{v}$ at $r = a+0.5$, the value of the radius midway between the inner and outer cylinders. (Figure 3 can be thought of as a plot of the velocity field on an imaginary cylinder at radius $r = a+0.5$ that is then unrolled on a flat surface.) The vertical height of figure 3 is equal to the axial wavelength $\lambda$, and the horizontal length is equal to the circumference midway between the inner and outer cylinders, or $2\pi(a+0.5)$. Figure 3 was scaled by multiplying all horizontal lengths and velocities by $\lambda/2\pi(a+0.5)$. The velocity field

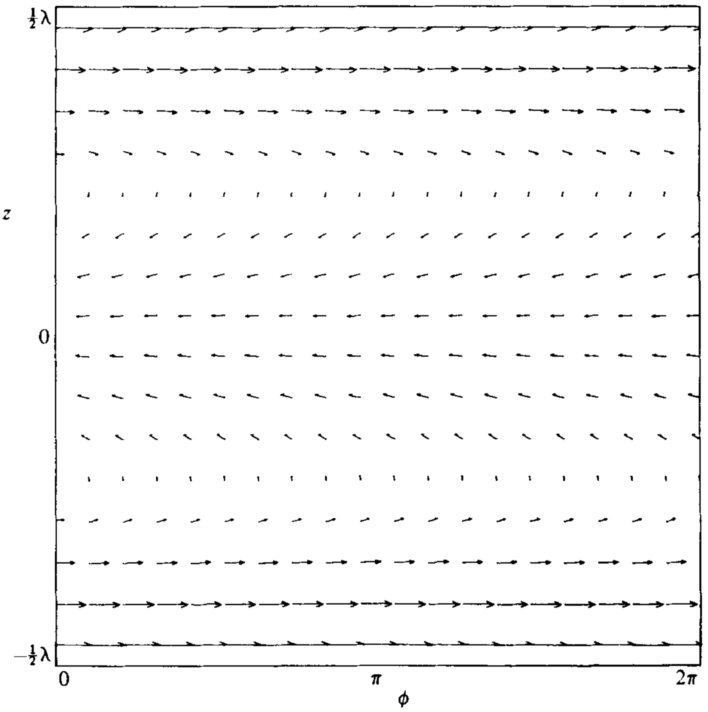

FIGURE 3. The 2-dimensional $(r,\phi)$-projection of the velocity field at $r = a+0.5$. The horizontal lengths and velocities are scaled by a factor of $\lambda/2\pi(a+0.5)$. The figure shows the velocity measured by an observer in a frame rotating with angular speed $c$, where $c$ is the azimuthal angular velocity of a fluid element located at the centre of one of the Taylor vortices shown in figure 2.

in figure 3 is not what an inertial observer would see. Instead, it is the velocity observed in a frame rotating with angular speed $c$, where $c$ is the azimuthal angular velocity of a fluid element in the centre of one of the Taylor vortices pictured in figure 2. The reason for this choice of reference frame will soon become apparent. The $z \rightarrow -z$, $v_z \rightarrow -v_z$ symmetry of (2.12)–(2.14) is evident in figure 3, which also shows clearly that in the $(z,\phi)$-plane there is large shear. Two inflection points are located very close to, but not exactly equal to, the values of $z$ that denote the centres of the Taylor vortices in figure 2. The precise location of the line of inflection in the shear velocity in the $(z,\phi)$-plane is, of course, a function of the radius at which the $(z,\phi)$-projection of the velocity is plotted.

In figure 4 we plot the mean (axially and azimuthally averaged) angular momentum $L(r) \equiv r\hat{v}_\phi(r, m = 0, k = 0)$ as a function of radius. The dimensionless angular momentum is always equal to zero at $b$ and to $\eta/(1-\eta)$ (or 7.00 for $\eta = 0.875$) at $a$. The solid curve is the angular momentum for stable Taylor-vortex flow, and the dotted curve represents unstable equilibrium circular Couette flow at the same values of $R$ and $\eta$. Figure 4 shows that Taylor-vortex flow increases the slope of $L(r)$ at the boundaries and reduces the gradient of $L(r)$ in the fluid interior. This change in $L(r)$ is exactly what is expected of a flow that transports angular momentum outward from the inner cylinder. The torque per unit axial length at the outer cylinder (see Part 1) is

$$G_{\text{out}} = -\frac{2\pi}{(1-\eta)R}\left.\frac{\partial L}{\partial r}\right|_{r=b}. \tag{3.1}$$

The steepening of the gradient of $L(r)$ at the boundaries causes the Taylor-vortex flow to exert more torque on the outer cylinder than the circular Couette flow exerts. The torque per unit axial length (in dimensionless units) of the unstable equilibrium circular Couette flow with $\eta = 0.875$ and $R = 1.179R_c$ is 2.6939; by contrast, the torque of the stable equilibrium Taylor-vortex flow with the same values of $\eta$ and $R$ and with $\lambda = 2.50$ is 3.3539. In §4 we show that, as the Reynolds number increases further, boundary layers form such that the gradient of $L(r)$ in the interior goes to zero and the gradient of $L(r)$ at the boundaries becomes still steeper.

In figure 5 we have plotted the energy $E(k)$ and enstrophy $\mathscr{E}(k)$ spectra as functions of axial harmonic number $k$:

$$E(k) \equiv \frac{c_k}{2\lambda^2}\int_a^b r\,\mathrm{d}r\int_0^{2\pi}\mathrm{d}\phi\left|\int_0^\lambda \mathrm{d}z\,\boldsymbol{v}(r,\phi,z)\,\mathrm{e}^{-2\pi \mathrm{i}kz/\lambda}\right|^2$$

$$= \tfrac{1}{2}c_k\int_a^b r\,\mathrm{d}r\int_0^{2\pi}\mathrm{d}\phi\,|\boldsymbol{v}(r,\phi,k)|^2, \tag{3.2}$$

$$\mathscr{E}(k) \equiv \frac{c_k}{2\lambda^2}\int_a^b r\,\mathrm{d}r\int_0^{2\pi}\mathrm{d}\phi\left|\int_0^\lambda \mathrm{d}z\,[\boldsymbol{\nabla}\times\boldsymbol{v}(r,\phi,z)]\,\mathrm{e}^{-2\pi \mathrm{i}kz/\lambda}\right|^2, \tag{3.3}$$

where
$$\boldsymbol{v}(r,\phi,k) \equiv \frac{1}{\lambda}\int_0^\lambda \mathrm{d}z\,\boldsymbol{v}(r,\phi,z)\,\mathrm{e}^{-2\pi \mathrm{i}kz/\lambda} \tag{3.4}$$

and where $c_k \equiv 2-\delta_{k,0}$. The use of $k$ in (3.4) is consistent with its use in (2.8). Equations (3.2) and (3.3) have normalization such that

$$E = \sum_{k=0}^{\infty} E(k), \qquad \mathscr{E} = \sum_{k=0}^{\infty}\mathscr{E}(k), \tag{3.5), (3.6}$$

where $E$ and $\mathscr{E}$ are the total energy and enstrophy per unit axial length. For a homogeneous isotropic flow we can plot the energy and enstrophy spectra as functions of a 3-dimensional wavevector. In a cylindrical geometry, however, those spectra as functions of a 3-dimensional harmonic number are not well-defined, so we have plotted 1-dimensional energy spectra. There are two interesting features of figure 5: the logarithms of the energy and enstrophy depend *linearly* on the axial harmonic number,

$$\ln[E(k)] \propto k^1, \tag{3.7}$$

and the spectra are very smooth and show no structure. Energy spectra for flows driven by thermal convection that have the same Reynolds number as the flow in figure 5 show structure in the form of bumps and wiggles (Marcus 1980). For $R < 10R_c$, all of the spectra of the numerically calculated Taylor-vortex flows and one-travelling-wave flows have smooth spectra without structure. To understand why flows driven by rotation have smoother spectra than flows driven by buoyancy, let us consider the time rate of change of $E(k)$. The value for $\dot{E}(k)$ is obtained from the scalar product of the axial Fourier component of the Navier–Stokes equation with the velocity, and is equal to

$$\dot{E}(k) = c_k\int_0^{2\pi}\mathrm{d}\phi\int_a^b r\,\mathrm{d}r\,\mathrm{Re}\left\{\frac{1}{\lambda}\int_0^\lambda \mathrm{d}z\,[-(\boldsymbol{v}\cdot\boldsymbol{\nabla})\,\boldsymbol{v}-\boldsymbol{\nabla}P]\cdot\boldsymbol{v}(r,\phi,-k)\,\mathrm{e}^{-2\pi \mathrm{i}kz/\lambda}\right\}$$

$$+c_kR^{-1}\int_0^{2\pi}\mathrm{d}\phi\int_a^b r\,\mathrm{d}r\,\mathrm{Re}\left\{\frac{1}{\lambda}\int_0^\lambda \mathrm{d}z\,\mathrm{e}^{-2\pi \mathrm{i}kz/\lambda}\,\boldsymbol{v}(r,\phi,-k)\cdot\nabla^2\boldsymbol{v}\right\}, \tag{3.8}$$

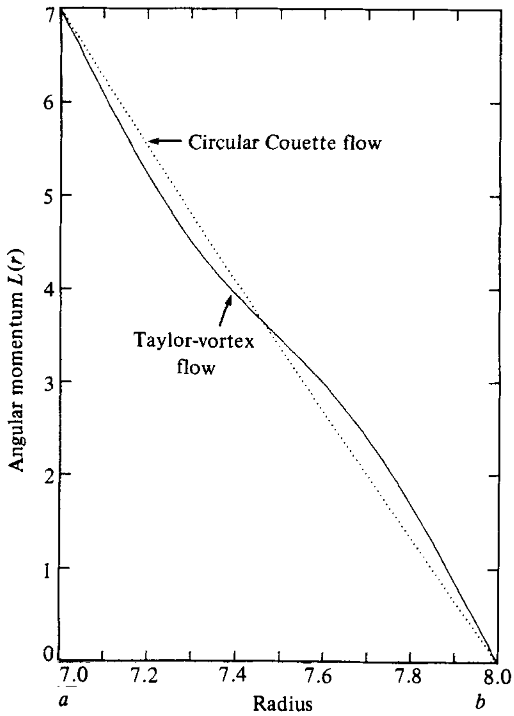

FIGURE 4. Angular momentum $L(r) \equiv r\bar{v}_{\phi}(r, m=0, k=0)$ as a function of radius for the stable Taylor-vortex flow in figures 2 and 3 (solid curve) and unstable circular Couette flow at the same $R$ and $\eta$ (dotted curve). Taylor-vortex flow has a steeper gradient of $L(r)$ at the boundaries, which indicates that the torque of Taylor-vortex flow is greater than the torque of circular Couette flow.

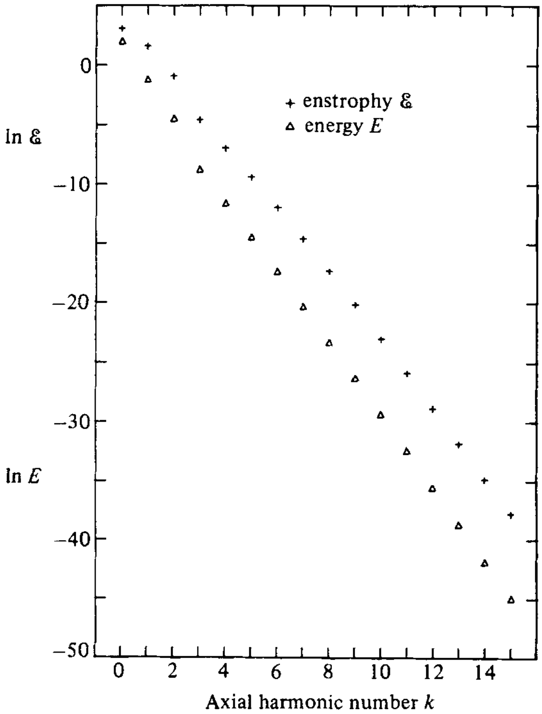

FIGURE 5. Energy $E(k)$ and enstrophy $\mathscr{E}(k)$ spectra as functions of the axial harmonic number $k$ for the flow in figures 2 and 3.

or equivalently

$$\begin{aligned}\dot{E}(k) = -\sum_{k'=\infty}^{\infty} c_k \int_0^{2\pi} \mathrm{d}\phi \int_a^b \mathrm{d}r\, r\, \mathrm{Re}\,\{ \mathrm{i}k' v_z(r,\phi,k-k')\, \boldsymbol{v}(r,\phi,k')\cdot \boldsymbol{v}(r,\phi,-k) \\ + \boldsymbol{v}(r,\phi,-k)\cdot[\boldsymbol{v}_{\mathrm{H}}(r,\phi,k-k')\cdot\boldsymbol{\nabla}_{\mathrm{H}}]\,\boldsymbol{v}(r,\phi,k')\} \\ -[2R^{-1}\mathscr{E}(k)+\delta_{k,0}4\pi R^{-1}]+\delta_{k,0}G_{\mathrm{in}}\Omega_{\mathrm{in}}, \qquad (3.9)\end{aligned}$$

where $G_{\mathrm{in}}$ is the torque per unit axial length that the inner cylinder exerts on the fluid, and $\boldsymbol{\nabla}_{\mathrm{H}}$ and $\boldsymbol{v}_{\mathrm{H}}$ are the 2-dimensional projections of the gradient and velocity;

$$\boldsymbol{\nabla}_{\mathrm{H}} = \boldsymbol{\nabla} - \hat{\boldsymbol{e}}_z \frac{\partial}{\partial z}, \qquad \boldsymbol{v}_{\mathrm{H}} = \boldsymbol{v} - \hat{\boldsymbol{e}}_z v_z. \qquad (3.10), (3.11)$$

The first two terms in (3.9) are a sum over all axial harmonic numbers $k'$, and corresponds to the nonlinear transfer of energy among modes with harmonic numbers $\pm k, k'$ and $\mp k-k'$. The transfer of energy among triads of modes is neither a source nor sink of energy. The next term in (3.9), $-[2R^{-1}\mathscr{E}(k)+\delta_{k,0}4\pi R^{-1}]$, is negative-definite and is due to the viscous dissipation. The only source of energy in (3.9) is the last term, $\delta_{k,0}G_{\mathrm{in}}\Omega_{\mathrm{in}}$. Equation (3.9) shows that in Taylor–Couette flow only the $k=0$ mode (in fact only the axisymmetric component of that mode) is driven directly by the torque applied to the inner cylinder. The $k=0$ mode receives energy at a rate of $G_{\mathrm{in}}\Omega_{\mathrm{in}}$, and it must lose this energy either directly by viscous dissipation or by transferring its energy to other modes by the nonlinear triad interaction. None of the $k \neq 0$ modes can gain energy directly from the imposed torque; they obtain it indirectly from the nonlinear interaction. For example, when circular Couette flow becomes unstable to a Taylor-vortex mode ($k=1$) the unstable mode grows at the expense of the energy in the $k=0$ component of the velocity. As each subsequent mode becomes unstable, it obtains its energy from the other velocity Fourier modes (including the axisymmetric $k=0$ mode) via the nonlinear triad interaction in (3.9). The axisymmetric $k=0$ mode dissipates directly most of the energy that enters it. Only a small fraction of $\dot{E}_{\mathrm{in}}$ is passed through nonlinear interactions to the $k \neq 0$ or $m \neq 0$ modes, even at large Reynolds number (see §5 and Appendix). By contrast, in thermal convection there is an additional source term in the equation for $\dot{E}(k)$ due to buoyancy. That term is proportional to $\mathrm{Re}\,[v_z(-k)\,T(k)]$, where $T(k)$ is the Fourier component of the temperature with axial harmonic number $k$. When a fluid first becomes unstable to thermal convection, a velocity mode and a temperature mode with the same wavelength are produced simultaneously. The kinetic energy of the mode is derived from the gravitational field, and the rate at which the buoyancy force converts potential to kinetic energy is proportional to the nonlinear heat flux or $\mathrm{Re}\,\{v_z(-k)\,T(k)\}$. Subsequent unstable modes can obtain their kinetic energy from *both* the kinetic energy of other velocity modes via the nonlinear triad interaction *and* directly from the potential energy via the $\mathrm{Re}\,\{v_z(-k)\,T(k)\}$ term.

We conjecture that $E(k)$ in figure 5 is smooth because the nonlinear interaction triad term in (3.9) has no intrinsic lengthscales and is only a function of the velocity energy spectrum. In thermal convection we found numerically (Marcus 1980) that the nonlinear heat flux varies significantly (and not smoothly) as a function of wavelength. (Presumably the variation is due to the fact that the heat flux depends sensitively on the spatial and temporal correlations of the velocity with the temperature.) Therefore it is not surprising that the energy spectrum of a thermally convecting fluid is not smooth.

Because Taylor-vortex flow is not turbulent, it is a mistake to think of the modes represented in figure 5 as physical eddies. Also, it is incorrect to compare the spectra in figure 5 with the dissipative regime of fully developed turbulence. Modes in the dissipation range of a turbulent flow have direct interaction with the modes in the inertial range, whereas the modes in the Taylor-vortex velocity are not supplied with energy from an inertial range.

Using the energy spectrum we can define the characteristic scalar velocity at harmonic number $k$ as

$$v(k) \equiv \left[ \frac{E(k)}{\int_0^{2\pi} \mathrm{d}\phi \int_a^b r\,\mathrm{d}r} \right]^{\frac{1}{2}}. \tag{3.12}$$

We can formally define a Kolmogorov axial wavenumber $k_{\mathrm{K}}$ such that the local Reynolds number at that wavenumber is equal to unity:

$$\frac{v(k_{\mathrm{K}})\,\lambda}{k_{\mathrm{K}}} \frac{da\Omega_{\mathrm{in}}}{\nu} = 1 \tag{3.13}$$

or

$$\frac{E(k_{\mathrm{K}})}{k_{\mathrm{K}}^2} = \frac{\pi}{\lambda^2} \frac{1+\eta}{1-\eta} R^{-2}. \tag{3.14}$$

For the flow in figure 5 $k_{\mathrm{K}} \approx 2.5$. Notice that there is no break in the spectrum at or near $k = k_{\mathrm{K}}$, since at $R = 139.32$ the entire spectrum is dissipative.

Using an approximate calculation (in which we ignore algebraic factors), we now show that the relation $\ln[E(k)] \propto |k|^1$ is reasonable and consistent with the Navier–Stokes equation. We also give an estimate for $\mathscr{E}(k) - E(k)$. Let us assume that the energy spectrum is of the form

$$E(k) = E_0\,\mathrm{e}^{-\gamma|k|^{\beta}}. \tag{3.15}$$

Since the enstrophy is proportional to the energy (and some spatial derivatives), we also assume

$$\mathscr{E}(k) = g(k)\,\mathrm{e}^{-\gamma|k|^{\beta}}, \tag{3.16}$$

where $g(k)$ is an algebraic function of $k$. We further assume that most of the energy that enters the set of modes with axial harmonic number $k$ via nonlinear interactions is viscously dissipated by that set of modes, and only a small fraction of the energy is passed on to other modes. The constant $\gamma$ (the slope of figure 5) is a measure of the fraction of energy that is passed on. As $|\gamma|$ increases, an exponentially smaller amount of energy is passed on. By equating the rate $\dot{E}_{\mathrm{in}}(k)$ at which energy enters the set of modes with axial harmonic number $k$ with the rate $\dot{E}_{\mathrm{out}}(k)$ at which energy is lost from the set, we can derive the value of $\beta$ in (3.15) and (3.16). The only net source of energy for $E(k)$ in (3.9) for modes with $k \neq 0$ is the nonlinear sum over $k'$. We shall assume that the only terms in that sum that are a *source* of energy (and not a sink of energy) are those terms that correspond to triad interactions of $v(-k)$, with modes that are *bigger* (in the axial direction) than $\lambda/|k|$ (i.e. modes with $|k'| < |k|$ and $|k'-k| < |k|$):

$$\dot{E}_{\mathrm{in}}(k) \approx \sum_{\substack{|k'|<|k| \\ |k-k'|<|k|}} f(k,k')\,|v(-k)|\,|v(k')|\,|v(k-k')| \int_0^{2\pi} \mathrm{d}\phi \int_a^b r\,\mathrm{d}r. \tag{3.17}$$

We have absorbed all of the geometrical factors and one spatial derivative into the form factor $f(k,k')$, which we assume depends algebraically but not exponentially on $k$ and $k'$. Using (3.12) and (3.15) with (3.17) yields

$$\dot{E}_{\mathrm{in}}(k) \approx \left(\pi \frac{1+\eta}{1-\eta}\right)^{-\frac{1}{2}} E_0^{\frac{1}{2}} \sum_{\substack{|k'|<|k| \\ |k-k'|<|k|}} f(k,k')\,E_0\,\mathrm{e}^{-\frac{1}{2}\gamma(|k|^{\beta}+|k'|^{\beta}+|k-k'|^{\beta}}. \tag{3.18}$$

If most of the energy is lost from the modes of harmonic number $k$ by dissipation then

$$\dot{E}_{\mathrm{out}}(k) \approx 2R^{-1}\mathscr{E}(k) = 2R^{-1}g(k)\,\mathrm{e}^{-\gamma|k|^{\beta}}. \tag{3.19}$$

Equating the exponent of $\dot{E}_{\mathrm{in}}(k)$ to the exponent of $\dot{E}_{\mathrm{out}}(k)$ yields $\beta = 1$, which agrees very well with the data (a straight line) in figure 5. Notice that setting $\beta$ equal to unity implies 'democracy' among the triad interactions; with $\beta = 1$ the rate of energy put into $v(-k)$ due to $v(k')$ and $v(k-k')$ is proportional to $\mathrm{e}^{-\frac{1}{2}\gamma(|k|+|k'|+|k-k'|)}$, but if $|k'| \leqslant |k|$ and $|k-k'| \leqslant |k|$ then

$$|k|+|k'|+|k-k'| = 2|k|, \tag{3.20}$$

and the rate of energy put into $v(-k)$ due to nonlinear interaction with $v(k')$ and $v(k-k')$ is proportional to $f(k,k')\,\mathrm{e}^{-\gamma|k|}$ and is *independent* of $k'$ (except for the algebraic factor in $f(k,k')$). Therefore all triad interactions in the nonlinear sum in (3.19) contribute equally to $\dot{E}_{\mathrm{in}}(k)$. Using (3.15) and (3.20), (3.18) becomes

$$\dot{E}_{\mathrm{in}}(k) \approx \left(\pi\frac{1+\eta}{1-\eta}\right)^{-\frac{1}{2}} E_0^{\frac{1}{2}}\,E(k) \sum_{\substack{|k'|<|k| \\ |k-k'|<|k|}} f(k,k'), \tag{3.21}$$

or $\dot{E}_{\mathrm{in}}(k) \propto E(k)$. Using (3.19) for $\dot{E}_{\mathrm{out}}(k)$ and (3.21) for $\dot{E}_{\mathrm{in}}(k)$ and equating the two, we obtain

$$\ln\mathscr{E}(k) - \ln E(k) = \ln R + \tfrac{1}{2}\ln\left[\frac{E_0}{4\pi}\frac{1-\eta}{1+\eta}\right] + \ln \sum_{\substack{|k'|<|k| \\ |k-k'|<|k|}} f(k,k'). \tag{3.22}$$

Fitting a least-squares line through the $k \neq 0$ points of $E(k)$ in figure 5 gives $\ln(E_0) \approx 5.2$. Using this value of $E_0$ and setting $\eta = 0.875$ and $R = 139.31$, (3.22) becomes

$$\ln\mathscr{E}(k) - \ln E(k) \approx 4.9 + \ln\left[\sum_{\substack{|k'|<|k| \\ |k-k'|<|k|}} f(k,k')\right]. \tag{3.23}$$

We expect the sum of the form factors to be near unity at $k = 1$ and to increase slowly (algebraically) with increasing $k$. Equation (3.23) therefore states that for small $k$ $\ln\mathscr{E}(k) - \ln E(k)$ should be approximately equal to 4.9 and slowly increase with $k$. The numerical data in figure 5 are in good agreement with (3.23).

### *Comparison between Taylor-vortex flow and circular Couette flow*

Throughout the remainder of this section and §4 we report on the values of the many physical properties, such as the energy and angular momentum, that characterize Taylor–Couette flows. To understand these flows it is necessary to compare the values of the properties of the different equilibrium flows. For example, the energy of the *stable* Taylor-vortex flow computed for some set of parameters $R$, $\eta$ and $\lambda$ should be compared to the energy of the *unstable* circular Couette flow computed for the same $R$ and $\eta$. The energy of the *stable* one-travelling-wave flow computed for some set of parameters $R$, $\eta$, $\lambda$ and $m_1$ should be compared with the energy of the *unstable* Taylor-vortex flow at the same $R$, $\eta$ and $\lambda$ and to the *unstable* circular Couette flow at the same $R$ and $\lambda$.

All of the properties of the circular Couette flow can be obtained analytically in closed form. These are summarized in table 1, which lists each quantity in 3 ways: (1) as a function of the radius ratio $\eta$ and Reynolds number $R$; (2) evaluated with

| Quantity | As functions of $\eta$ and $R$ | As functions of $R/R_c$ evaluated at $\eta = 0.875$ $(R_c \equiv 118.16)$ | As functions of $R/R_c$ and $1-\eta$ in the limit $\eta \rightarrow 1$ |
|---|---|---|---|
| $E(\mathrm{CC})$ | $\dfrac{\pi\eta^2}{(1-\eta)^3(1+\eta)}\left[\dfrac{\eta^2-3}{4}-\dfrac{\ln\eta}{1-\eta^2}\right]$ | 7.32 | $\dfrac{\pi}{3(1-\eta)}$ |
| $\mathscr{E}(\mathrm{CC})$ | $\dfrac{2\pi\eta^2}{1-\eta^2}$ | 20.5 | $\dfrac{\pi}{1-\eta}$ |
| $\mathscr{L}(\mathrm{CC})$ | $\dfrac{\pi\eta(1+\eta)}{2(1-\eta)^2}$ | 165 | $\dfrac{\pi}{(1-\eta)^2}$ |
| $G(\mathrm{CC})$ | $\dfrac{4\pi\eta}{(1-\eta)(1-\eta)^2 R}$ | $3.18\left(\dfrac{R}{R_c}\right)^{-1}$ | $0.152(1-\eta)^{-\frac{3}{2}}\left(\dfrac{R}{R_c}\right)^{-1}$ |
| $\dot{E}(\mathrm{CC})$ | $\dfrac{4\pi\eta}{(1-\eta^2)R}$ | $0.454\left(\dfrac{R}{R_c}\right)^{-1}$ | $0.152(1-\eta)^{-\frac{1}{2}}\left(\dfrac{R}{R_c}\right)^{-1}$ |
| $\tau_E(\mathrm{CC}) \equiv E(\mathrm{CC})/\dot{E}(\mathrm{CC})$ | $\dfrac{R\eta^2}{4(1-\eta)^2}\left[\dfrac{\eta^2-3}{4}-\dfrac{\ln(\eta)}{1-\eta^2}\right]$ | $16.1\left(\dfrac{R}{R_c}\right)$ | $6.90(1-\eta)^{-\frac{1}{2}}\left(\dfrac{R}{R_c}\right)$ |
| $\tau_{\mathscr{L}}(\mathrm{CC}) \equiv \mathscr{L}(\mathrm{CC})/G(\mathrm{CC})$ | $\frac{1}{8}(1+\eta)^2 R$ | $51.9\left(\dfrac{R}{R_c}\right)$ | $20.7(1-\eta)^{-\frac{1}{2}}\left(\dfrac{R}{R_c}\right)$ |
| $\tau_\mathrm{p}$ | $\dfrac{2\pi\eta}{1-\eta}$ | 44.0 | $\dfrac{2\pi}{1-\eta}$ |
| $\tau_\nu$ | $R$ | $118\left(\dfrac{R}{R_c}\right)$ | $41.4(1-\eta)^{-\frac{1}{2}}\left(\dfrac{R}{R_c}\right)$ |
| $\tau_E(\mathrm{CC})/\tau_\nu$ | $\dfrac{\eta^2}{4(1-\eta)^2}\left[\dfrac{\eta^2-3}{4}-\dfrac{\ln(\eta)}{1-\eta^2}\right]$ | 0.136 | $\frac{1}{6}$ |
| $\tau_{\mathscr{L}}(\mathrm{CC})/\tau_\nu$ | $\frac{1}{8}(1+\eta)^2$ | 0.439 | $\frac{1}{2}$ |
| $\tau_E(\mathrm{CC})/\tau_\mathrm{p}$ | $\dfrac{R\eta}{8\pi(1-\eta)^3}\left[\dfrac{\eta^2-3}{4}-\dfrac{\ln\eta}{1-\eta^2}\right]$ | $0.367\left(\dfrac{R}{R_c}\right)$ | $1.10(1-\eta)^{\frac{1}{2}}\left(\dfrac{R}{R_c}\right)$ |
| $\tau_{\mathscr{L}}(\mathrm{CC})/\tau_\mathrm{p}$ | $\dfrac{(1+\eta)^2 R}{16\pi\eta(1-\eta)}$ | $1.18\left(\dfrac{R}{R_c}\right)$ | $3.30(1-\eta)^{\frac{1}{2}}\left(\dfrac{R}{R_c}\right)$ |

TABLE 1. Physical properties of circular Couette flow (1) as arbitrary functions of $\eta$ and $R$, (2) evaluated at $\eta = 0.875$ with $R_c = 118.16$, and (3) as functions of $R/R_c$ and $1-\eta$ in the limit $\eta \rightarrow 1$. In the limit $\eta \rightarrow 1$, $R_c \approx 41.41(1-\eta)^{-\frac{1}{2}}$

$\eta = 0.875$ but as a function of $R$; and (3) as a function of $R/R_c$ and $1-\eta$ in the limit $\eta \rightarrow 1$. In the limit $\eta \rightarrow 1$ we can approximate $R_c$ by (Chandrasekhar 1961)

$$R_c \simeq 41.41(1-\eta)^{-\frac{1}{2}}. \tag{3.24}$$

The notation CC used in table 1 denotes that the quantity is computed for equilibrium circular Couette flow. The kinetic energy $E$, enstrophy $\mathscr{E}$, angular momentum $\mathscr{L}$, torque $G$ and the rate $\dot{E}$ at which kinetic energy is put into (or is dissipated by) the flow are all evaluated per unit axial length of the cylinder. For example, the enstrophy is defined

$$\mathscr{E} \equiv \frac{1}{2}\int_a^b r\,\mathrm{d}r \int_0^{2\pi} \mathrm{d}\phi \int_0^{\lambda} \mathrm{d}z\,(\nabla \times v)^2/\lambda. \tag{3.25}$$

In a steady state $G \equiv G_\mathrm{in} \equiv G_\mathrm{out}$, $\dot{E} \equiv \dot{E}_\mathrm{in} \equiv \dot{E}_\mathrm{out}$ and

$$\dot{E} = \frac{2}{R}(\mathscr{E}+2\pi) = G\Omega_\mathrm{in}. \tag{3.26}$$

Note that in our dimensionless units $\mathscr{L}(\mathrm{CC})$, $E(\mathrm{CC})$ and $\mathscr{E}(\mathrm{CC})$ are independent of $R$. For the Taylor–Couette flows it is useful to define four characteristic timescales.

The energy timescale is defined to be the time it would take the motor that drives the inner cylinder with power $\dot{E}$ to completely replenish the energy $E$ stored in the flow, or

$$\tau_E \equiv E/\dot{E}. \tag{3.27}$$

The momentum timescale is defined to be the time needed for the external torque $G$ to replace the angular momentum $\mathscr{L}$, or

$$\tau_{\mathscr{L}} \equiv \mathscr{L}/G. \tag{3.28}$$

The timescales $\tau_E$ and $\tau_{\mathscr{L}}$ for circular Couette flow are both given in table 1. Two other important timescales listed in table 1 are the dynamical time or the rotation period of the inner cylinder $\tau_\mathrm{p}$ and the diffusion timescale $\tau_\nu \equiv (b-a)^2/\nu$. The values of the diffusion and dynamical timescales are uniquely determined by the Reynolds number and the radius ratio, and are therefore both independent of the type of flow (i.e. wavy-vortex, circular Couette, etc.). In fact, in our dimensionless units $\tau_\nu$ is identically equal to $R$. As shown in table 1, in circular Couette flow the angular-momentum and energy timescales in units of the viscous timescale, $\tau_{\mathscr{L}}(\mathrm{CC})/\tau_\nu$ and $\tau_E(\mathrm{CC})/\tau_\nu$, depend only on $\eta$ and are independent of $R$. For small gaps $\tau_{\mathscr{L}}(\mathrm{CC})/\tau_\nu$ and $\tau_E(\mathrm{CC})/\tau_\nu$ are independent of both $1-\eta$ and $R/R_\mathrm{c}$ and are equal to $\frac{1}{2}$ and $\frac{1}{6}$ respectively. Table 1 also shows that for $\eta = 0.875$ if $R/R_\mathrm{c}$ is near unity then the angular-momentum timescale $\tau_{\mathscr{L}}$ and the inner-cylinder rotation period $\tau_\mathrm{p}$ are approximately the same.

The physical properties of the steady-state stable Taylor-vortex flow (denoted by TV) at $\eta = 0.875$, $\lambda = 2.50$ and $R = 1.179R_\mathrm{c}$ are summarized in table 2. Each quantity $Q$ is given in dimensionless units and in units of $Q(\mathrm{CC})$. As already shown in figure 4, the torque $G$ is increased substantially in the Taylor-vortex flow; for $R = 1.179R_\mathrm{c}$ it is 24 % greater than the torque of circular Couette flow. Since $\dot{E}(\mathrm{TV})$ is proportional to $G(\mathrm{TV})$, the rate at which energy enters (or is dissipated by) the Taylor-vortex flow is also 24 % greater than $\dot{E}(\mathrm{CC})$. Furthermore, since $\mathscr{E}(\mathrm{TV})$ is a monotonic function of $\dot{E}(\mathrm{TV})$ (see equation (3.26)), $\mathscr{E}(\mathrm{TV})/\mathscr{E}(\mathrm{CC})$ is also greater than unity. As $R$ increases, the ratios $G(\mathrm{TV})/G(\mathrm{CC})$, $\dot{E}(\mathrm{TV})/\dot{E}(\mathrm{CC})$ and $\mathscr{E}(\mathrm{TV})/\mathscr{E}(\mathrm{CC})$ all continue to increase.

During the initial-value experiment in which we start with the unstable equilibrium circular Couette flow and let it change to the stable Taylor-vortex flow, boundary layers form in the mean angular-momentum profile $L(r)$ (see figure 4). The boundary layer always forms at the outer cylinder before the inner, resulting in the torque $G_\mathrm{out}$ at the outer cylinder being greater than the torque $G_\mathrm{in}$ at the inner cylinder for several inner-cylinder rotation periods while the flow comes into equilibrium. When $G_\mathrm{out} > G_\mathrm{in}$ the flow loses angular momentum (see equation (3.5) of Part 1). Therefore the angular momentum $\mathscr{L}(\mathrm{TV})$ of the Taylor-vortex flows is less than $\mathscr{L}(\mathrm{CC})$. For $R = 1.179R_\mathrm{c}$, $\mathscr{L}(\mathrm{TV})$ is about 1 % less than $\mathscr{L}(\mathrm{CC})$. Since most of the kinetic energy of Taylor-vortex flow resides in the $k = 0$, $m = 0$ azimuthal component of the velocity (see below), if $\mathscr{L}(\mathrm{TV})/\ell(\mathrm{CC}) < 1$, then we should also expect $E(\mathrm{TV})/E(\mathrm{CC}) < 1$. For $R = 1.179R_\mathrm{c}$, $E(\mathrm{TV})$ is about 2 % lower than $E(\mathrm{CC})$. As $R$ increases, $\mathscr{L}(\mathrm{TV})/\mathscr{L}(\mathrm{CC})$ and $E(\mathrm{TV})/E(\mathrm{CC})$ continue to decrease.

Because $E(\mathrm{TV})/E(\mathrm{CC}) < 1$ and $\dot{E}(\mathrm{TV})/\dot{E}(\mathrm{CC}) > 1$, the energy timescale for Taylor-vortex flow, $\tau_E(\mathrm{TV})$, is less than $\tau_E(\mathrm{CC})$ by about 22 %. Similarly, $\mathscr{L}(\mathrm{TV})/\mathscr{L}(\mathrm{CC}) < 1$ and $G(\mathrm{TV})/G(\mathrm{CC}) > 1$ imply that $\tau_{\mathscr{L}}(\mathrm{TV})/\tau_{\mathscr{L}}(\mathrm{CC}) < 1$. As $R$ increases, $\tau_E(\mathrm{TV})/\tau_E(\mathrm{CC})$ and $\tau_{\mathscr{L}}(\mathrm{TV})/\tau\mathscr{L}(\mathrm{CC})$ continue to decrease. The fact that $\tau_{\mathscr{L}}$ is nearly identical with the inner-cylinder rotation period $\tau_\mathrm{p}$ is purely coincidental and is due to our choice of $\eta$ (see table 1).

| Quantity | Dimensionless units | Divided by the same quantity for circular Couette flow with $\eta = 0.875$, $R/R_c = 1.17$ |
|---|---|---|
| $E$ | 7.14 | 0.976 |
| $\mathscr{E}$ | 27.1 | 1.32 |
| $\mathscr{L}$ | 163 | 0.988 |
| $G$ | 3.35 | 1.24 |
| $\dot{E}$ | 0.479 | 1.24 |
| $\tau_E$ | 14.9 | 0.784 |
| $\tau_{\mathscr{L}}$ | 48.6 | 0.793 |
| $\tau_E/\tau_\nu$ | 0.107 | — |
| $\tau_{\mathscr{L}}/\tau_\nu$ | 0.349 | — |
| $\tau_E/\tau_p$ | 0.339 | — |
| $\tau_{\mathscr{L}}/\tau_p$ | 1.10 | — |

TABLE 2. Summary of physical properties for Taylor-vortex flow with $\eta = 0.875$, $R_c = 118.16$, $R/R_c = 1.179$, $\lambda = 2.50$

For a Reynolds number of 139.32 or $1.179R_c$, most of the kinetic energy is still in the azimuthal component of the velocity with only about 0.1 % in the radial component and 0.2 % in the axial component. These low percentages are surprising, since approximately 4 % of the total kinetic energy is in the Taylor-vortex velocity (i.e. components of the velocity with $k \neq 0$). We conclude that most of the energy of the Taylor vortex itself is in the azimuthal direction rather than the radial or axial directions.

### *Stability boundaries of Taylor-vortex flow in $(R, \lambda)$-parameter space*

As discussed in Part 1, we find that the numerically computed stability boundaries of Taylor-vortex flow agree well with the experimentally observed values. Holding $\lambda$ fixed, we find that if the Reynolds number decreases below a critical value then the Taylor-vortex flow decays into circular Couette flow. The critical value is the usual one that is found by determining where circular Couette flow becomes neutrally stable to linear perturbations. If we begin with a one-travelling-wave flow with $m_1 = 6$ and decrease $R$ while holding $\lambda$ fixed, we find that there is a transition from $m_1 = 6$ to $m_1 = 4$. The Reynolds number for transition is a function of $\lambda$ and our numerical results are in good agreement with the laboratory experiments of King & Swinney (1983).

With our present initial-value code we cannot determine the stability boundaries when $R$ is held fixed and $\lambda$ is continuously varied. We remind the reader that our code cannot compute transitions where the number $N$ of vertically stacked Taylor vortices changes. Our code uses discrete Fourier sums; if the code represented the velocity as a continuous Fourier integral it would allow transitions to any value of $N$. Our calculations are done with a prescribed value of $\lambda$. However, because we represent the flow spectrally with the truncated sum

$$v(r, \phi, z, t) = \sum_{k=0}^{K} f(r, \phi, k, t)\, e^{2\pi i k z/\lambda}, \tag{3.29}$$

there can be a transition from a flow with axial wavelength $\lambda$ to a flow with axial wavelength $\frac{1}{2}\lambda$, which has $f(r, \phi, k, t) \equiv 0$ for all $k$ equal to odd integers. Transitions with axial-wavelength halving are not observed experimentally; the observed transitions change the number $N$ of vortices by two. Nonetheless, as we slowly increase $\lambda$ we find that there is an abrupt transition from a flow with axial wavelength $\lambda$ to one with wavelength $\frac{1}{2}\lambda$ whenever $\lambda$ increases above some critical value. This numerically computed critical value of $\lambda$ is a function of $R$ and is nearly equal to the observed critical value of $\lambda$ where $N$ changes to $N+2$. The similarity between the observed and the numerically determined values of the critical wavelength leads us to the conclusion that the physical processes responsible for the real transitions are approximated well by our discrete Fourier representation of the velocity.

## 4. Numerical simulation of the one-travelling-wave flow

### *A stable equilibrium flow with* $\eta = 0.875$, $\lambda = 3.00$, $m_1 = 6$, $R = 2.063R_c$

We have calculated several one-travelling-wave flows using 33 radial Chebyshev polynomials, 32 axial Fourier modes, and 32 azimuthal Fourier modes where we exploit the shift-and-reflect symmetry and $m_1$ fold rotation symmetry of the flows. We report first on the numerical results of a flow with $m_1 = 6$, $\lambda = 3.00$, $\eta = 0.875$ and $R = 243.81 = 2.063R_c$. In figure 6 we have plotted the 2-dimensional projection of the velocity in the $(r, z)$-plane (inner cylinder on left and outer cylinder on right). Each of the nine plots shown in figure 6 is for a different value of $\phi$, with the first arbitrarily labelled as $\phi = 0$. Each of the other figures are equally spaced in $\phi$, with the last at $\phi = \pi/m_1$. It is unnecessary to plot the figures for $\phi > \pi/m_1$, owing to the shift-and-reflect symmetry of the flow: the plot of the velocity field at $\phi = (2\pi/96) \times 9$ is the same as the plot at $\phi = (2\pi/96) \times 1$ reflected about $z = 0$ (i.e. upside-down). The inflow boundary in figure 6 is always near $z = 0$, and the outflow boundary is always near $z = \pm\frac{1}{2}\lambda$. Similar to Taylor-vortex flow (see figure 2), the one-travelling-wave flow has a larger radial velocity at the outflow boundary than it has at the inflow boundary.

In figure 6 we see that for each value of $\phi$ one of the Taylor vortices is diminished and one is enhanced. For $\phi = (2\pi/96) \times 6$ the bottom counterclockwise vortex has nearly disappeared. For each value of $\phi$ there is also a large axial component of velocity; at $\phi = 0$ in figure 6 there is a strong upward flow in the axial direction. The solid curves are contours showing the surfaces where the azimuthal component of the velocity is constant. For each figure we plot only one contour – the surface where the fluid has the same azimuthal angular velocity $s_1$ as the travelling wave. All fluid to the left of the curve is moving faster than the travelling wave and all fluid to the right is slower. The solid curves always pass near the centre of at least one of the vortices; at the critical Reynolds number for the onset of one-travelling-wave flow the solid curve passes through the exact centres of both vortices (see below).

To understand better the travelling-wave flow in figure 6, we have plotted in figure 8 the $(r, z)$-projection of the axisymmetric *unstable* Taylor-vortex flow computed with the same values of $\eta$, $R$ and $\lambda$ as the wavy Taylor-vortex flow in figure 6. The solid curve is the contour where the azimuthal velocity is $s_1$. Figure 7 shows the velocity field of the wavy-vortex flow in figure 6 with the velocity field of the Taylor-vortex flow in figure 8 subtracted from it. (The solid curves in figure 7 are identical with those in figure 6.) If the Reynolds number of the flow were infinitesimally greater than the critical value for the onset of travelling waves (so that the non-axisymmetric component of the velocity had an infinitesimal amplitude) then the flow plotted in figure 7 would be exactly equal to the first unstable non-axisymmetric eigenmode of the Taylor-vortex flow in figure 8. We can think of the flow in figure 7 as a 'nonlinear travelling eigenmode'. In the $(r, z)$-plane the nonlinear travelling mode appears as a vortex (see figure 7, $\phi = (2\pi/96) \times 6$) whose axial length is about twice as long as

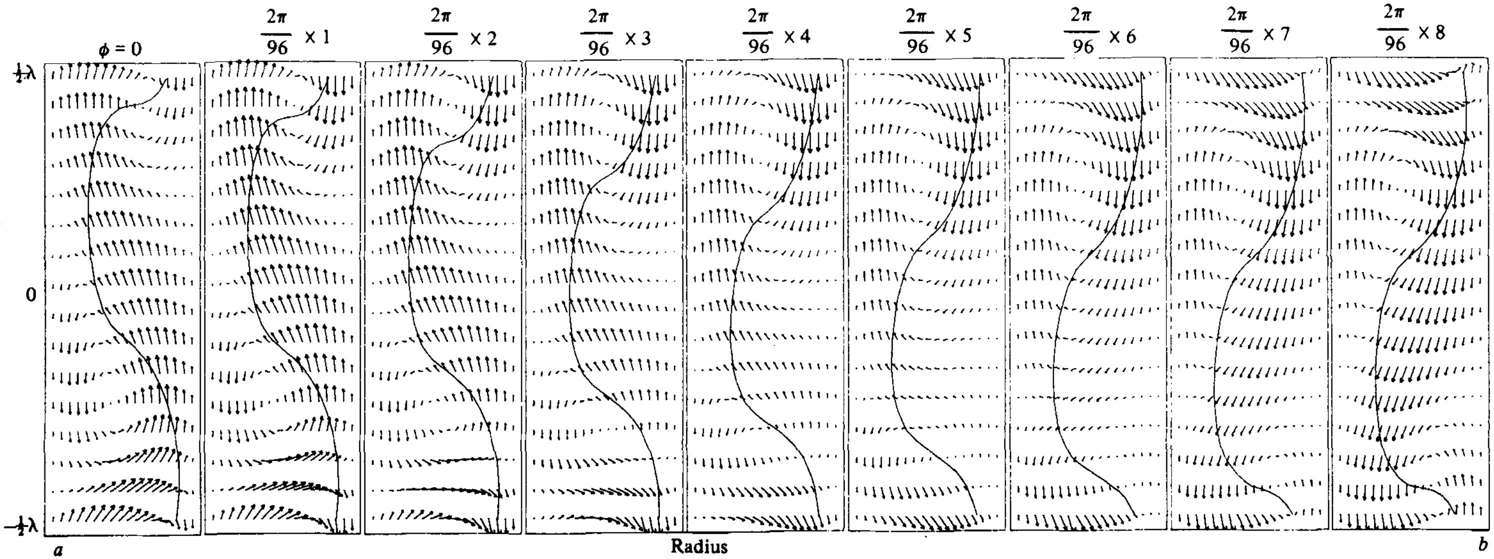

FIGURE 6. The $m_1 = 6$, $R = 2.063R_e$, $\lambda = 3.00$, $\eta = 0.875$ one-travelling-wave flow projected onto the $(r, z)$-plane for $\phi = (2\pi/16m_1)\,i$, for $i = 0, \ldots, 8$. For each figure the outer cylinder is on the right and the inner cylinder is on the left. The shift-and-reflect symmetry requires that $v_r(\phi = 0, z) = v_r(\phi = \pi/m_1, -z)$ and $v_z(\phi = 0, z) = -v_z(\phi = \pi/m_1, -z)$. The solid curve passes through all fluid with azimuthal velocity equal to the speed of the travelling wave.

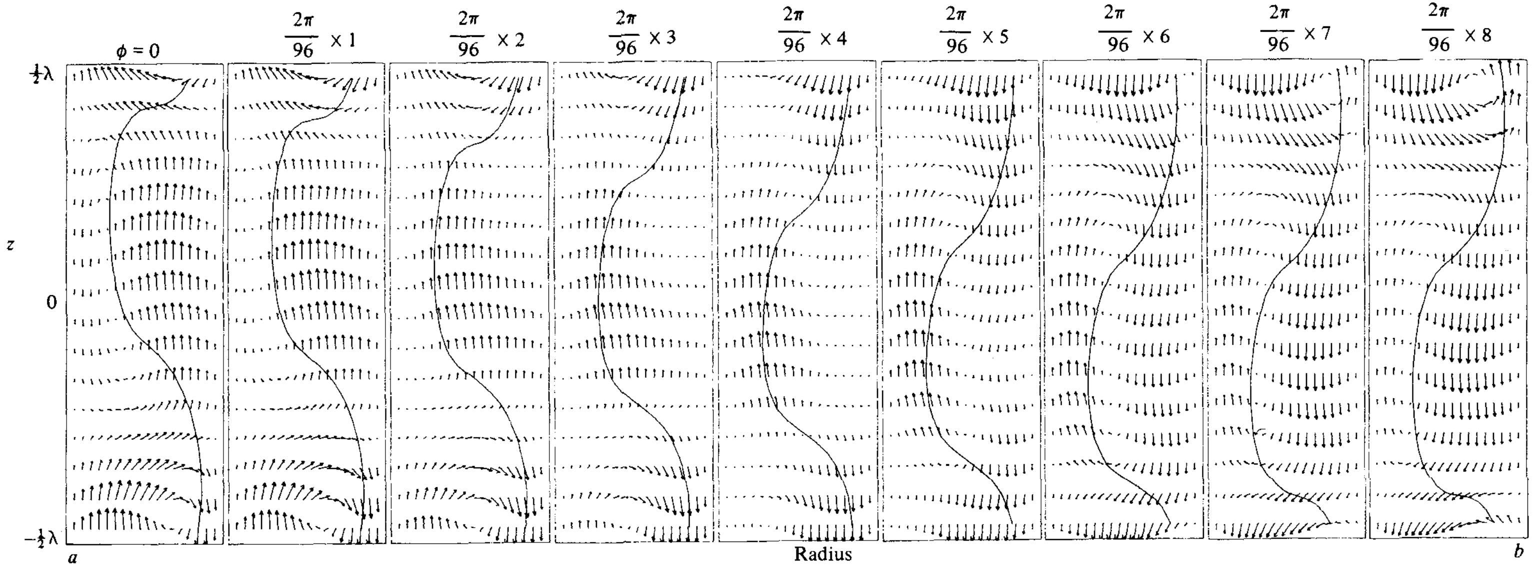

Figure 7. The nonlinear travelling mode equal to the velocity in figure 6 minus the unstable equilibrium Taylor-vortex velocity in figure 8.

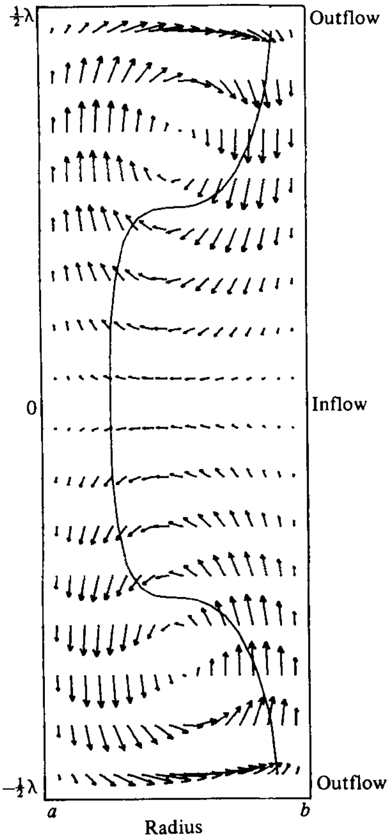

FIGURE 8. The $(r, z)$-projection of the axisymmetric velocity of the unstable equilibrium Taylor-vortex flow with the same $R$, $\eta$ and $\lambda$ as the flow in figure 6.

that of vortices of the one-travelling-wave flow (figure 6) or the Taylor-vortex flow (figure 8). In §3 we showed that in Taylor-vortex flow the fluid near the centres of the vortices never mixes with the surrounding fluid near the boundaries or in the neighbouring vortices. Figures 7 and 8 show that the nonlinear travelling mode mixes the fluid at the centres of adjacent Taylor vortices. Figure 8 shows that the separation between the Taylor vortices is much greater at the inflow boundary than at the outflow boundary. The large vortex of the nonlinear travelling wave always connects and mixes together a pair of Taylor vortices across their inflow boundary and *never* their outflow boundary. The large vortices change their direction as a function of $\phi$; the shift-and-reflect symmetry of the flow guarantees that the large clockwise vortex at $\phi = (2\pi/96) \times 7$ in figure 7 appears as a large counterclockwise vortex at $\phi = (2\pi/96) \times 15$. For some values of $\phi$ the nonlinear travelling mode also contains a very small vortex, which rotates in the direction opposite to that of the larger vortex (see the bottom of figure 7 at $\phi = (2\pi/96) \times 1$). The small vortex of the nonlinear travelling mode is always located at the outflow boundary between the Taylor vortices, and never at the inflow boundary. (This small vortex is not a numerical artefact. We remind the reader that the spacing of the arrows shown in figure 7 does not correspond to the numerical resolution of the calculation.)

In figure 9 we have plotted the 2-dimensional projection of the one-travelling-wave velocity in the $(z, \phi)$-plane at $r = a + 0.5$, the point midway between the inner and

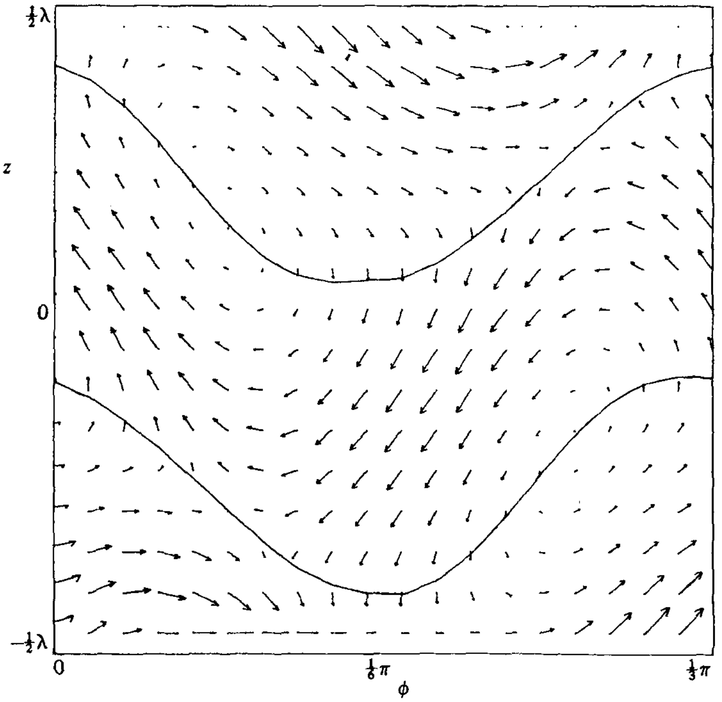

FIGURE 9. $(z, \phi)$-projection of the one-travelling-wave flow shown in figure 6. The plotted velocity is that seen by an observer in a frame rotating with speed $s_1$, the travelling-wave speed. The solid curves pass through all fluid with $v_\phi = 0$ in this frame.

outer cylinders. In the figure $-\frac{1}{2}\lambda \leqslant z \leqslant \frac{1}{2}\lambda$ and $0 \leqslant r\phi \leqslant 2\pi(a+0.5)/m_1$, so all lengths and velocities in the azimuthal direction have been scaled by a factor of $\lambda m_1/2\pi(a+0.5)$. The velocity is that measured by an observer in a frame rotating with speed $s_1$. The solid curves are similar to those in figure 6 and pass through all points with $v_\phi = 0$ (in the rotating frame).

We have subtracted the axisymmetric, unstable, equilibrium Taylor-vortex flow for $R = 2.063R_c$, $\eta = 0.875$ and $\lambda = 3.00$ from figure 9 and plotted the difference, or the $(z, \phi)$-projection of the nonlinear travelling mode, in figure 10. It appears as a 2-dimensional array of vortices with alternating signs. (We remind the reader that figure 10 should be repeated periodically in both the horizontal and vertical directions.) By plotting figures similar to figure 10 at different values of radius, we have determined that, as the radius of the projection increases, the vortices with centres near $z = 0$ (or between the two solid curves in figure 10) shift to the left (i.e. the centres remain near $z = 0$ but with decreasing values of $\phi$). The total shift in $\phi$ of the vortices centred near $z = 0$ is approximately $\pi/m_1$ as the radius of the $(z, \phi)$-projection increases from $a$ to $b$. The vortices centred near $z = \pm\frac{1}{2}\lambda$ also shift to the left as the radius of the projection increases from $a$ to $b$, but not at the same rate as the vortices near $z = 0$. Figure 10 shows that at $r = a+0.5$, the vortices near $z = 0$ are midway (in $\phi$) between the vortices near $z = \pm\frac{1}{2}\lambda$. Projections of the velocity at radii close to the outer and inner cylinders show that the vortices near $z = 0$ and $z = \pm\frac{1}{2}\lambda$ are centred at common values of $\phi$.

The inflow and outflow boundaries of the Taylor vortices with one travelling wave have been measured experimentally (cf. DiPrima & Swinney 1981). The vortex boundaries are visualized by suspending in the fluid flat flakes that align themselves

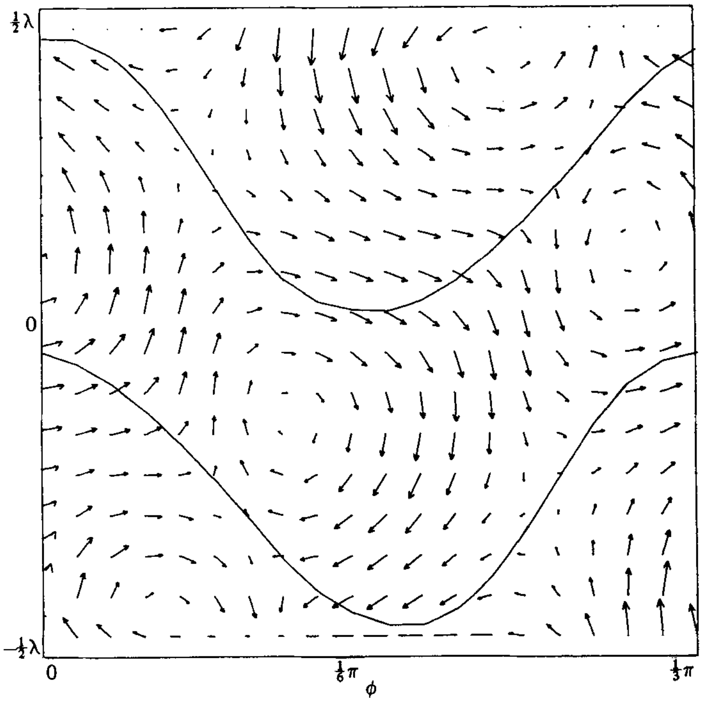

FIGURE 10. The nonlinear travelling mode equal to the velocity in figure 9 minus the unstable equilibrium Taylor-vortex velocity.

in the direction of the local stress. Motion along the observer's line of sight (radial motion) appears dark, while motion perpendicular to the line of sight appears light. Although the visualization does not correspond to a mathematically well-defined quantity, we have tried to reproduce qualitatively the flow visualization due to the suspended flakes. In figure 11 we have plotted contours of the two local maxima of the ratio of kinetic energy in the radial direction to the sum of the kinetic energies in the azimuthal and axial directions (integrated over all radii). When this ratio is very large the fluid is moving along the observer's line of sight and the maxima should correspond to the dark inflow/outflow boundaries seen in the experiments. Two features of figure 11 agree qualitatively with the experimental observations: first, the $z$ coordinate of the inflow boundary varies less with $\phi$ than it does for the outflow boundary; secondly, the inflow boundary lags behind the outflow boundary (i.e. if the minimum value of $z$ in the inflow boundary occurs at $\phi = \phi_{\text{min, in}}$ and the minimum value of $z$ in the outflow boundary occurs at $\phi = \phi_{\text{min, out}}$, then $\phi_{\text{min, in}} < \phi_{\text{min, out}}$).

Figures 12 and 13 show the 2-dimensional projection in the $(z, \phi)$-plane of the contours of equal energy and enstrophy. These two figures are evaluated at the radius midway between the inner and outer cylinders, and the plots are scaled as in figure 9. Although the equienergy surfaces in figure 12 reflect the $(z, \phi)$-dependence of the inflow and outflow boundaries, there is no strong spatial concentration of the energy at the boundaries. On the other hand, the equienstrophy surfaces are strongly concentrated at the outflow boundary near $z = \frac{1}{2}\lambda$ and, to a lesser degree, at the inflow boundaries at $z = 0$ and $z = \lambda$.

Although figures 12 and 13 show that the spatial structures of the energy and enstrophy are very different, the spectra of the energy and enstrophy with respect

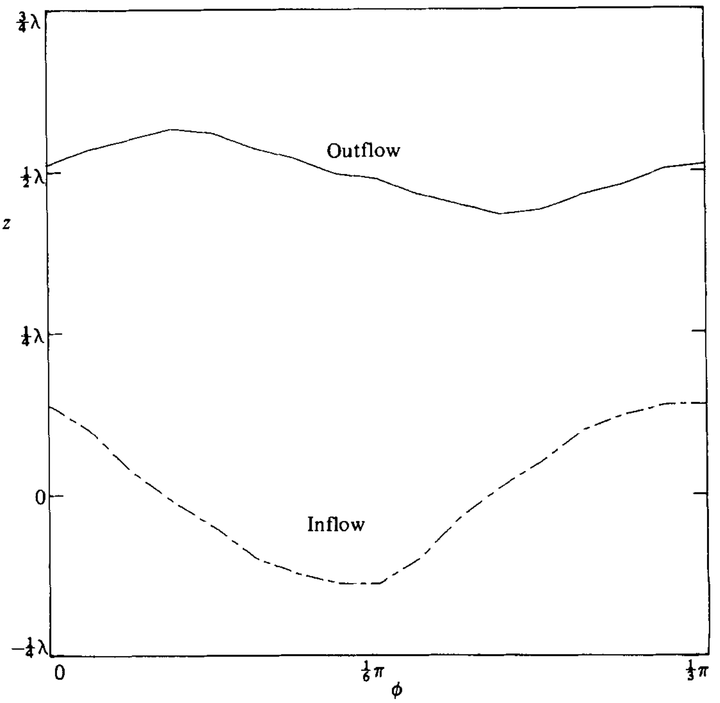

FIGURE 11. Inflow and outflow boundaries between the Taylor vortices of the flow in figures 6 and 9. The boundaries are computed by finding the local maxima of $\int v_r^2/(v_\phi^2+v_z^2)\,\mathrm{d}r$.

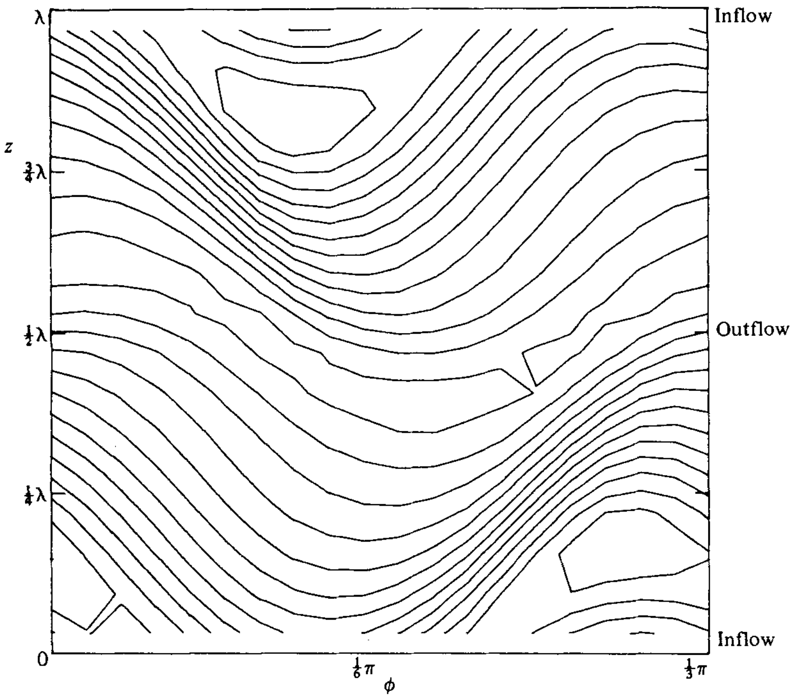

FIGURE 12. Projection onto the $(z, \phi)$-plane at $r = a+0.5$ of the equienergy surfaces of the one-travelling-wave flow shown in figure 6 and 9.

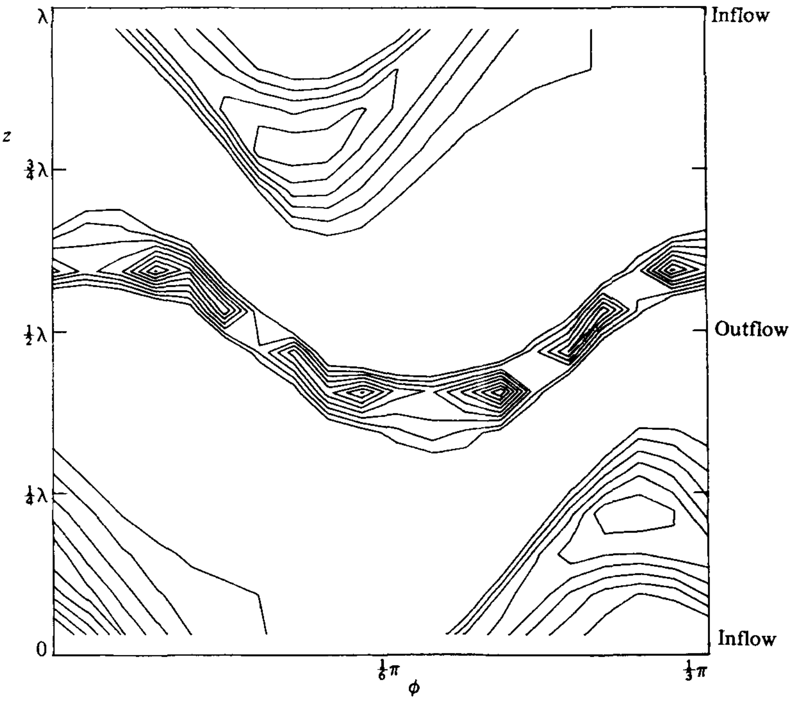

FIGURE 13. Same as figure 12 for the equienstrophy surfaces. Most of the enstrophy is at the outflow boundary.

to axial wavenumber $k$, shown in figure 14, look very similar. The logarithms of the energy and enstrophy are both linear in $k$, and the spectra of the one-travelling-wave flow are similar to the spectra of the axisymmetric Taylor-vortex flow (see figure 5). Figure 14 shows that there is a small departure from linearity in the one-travelling-wave flow's spectra at the lowest wavenumbers. (The figure also shows a slight upward curl at the largest wavenumber – this is a numerical artefact due to the insufficient resolution; doubling the spatial resolution removes the upward curl at $k = 15$.) Figure 14 should be compared with figure 15, which shows the energy and enstrophy spectra of the unstable, axisymmetric, equilibrium, Taylor-vortex flow computed with the same $R$, $\eta$ and $\lambda$ as figure 14. The fall-off of the energy and enstrophy with increasing axial wavenumber is faster for the non-axisymmetric one-travelling-wave flow than for the Taylor-vortex flow, resulting in a larger $E(k)$ and $\mathscr{E}(k)$ at high wavenumber for the latter flow. This faster rate of fall-off and lack of energy in the high-axial-wavenumber modes is due to the fact that the one-travelling-wave flow has a viscous dissipation term in (3.8) that is proportional to $m_1^2/R$. This dissipation is absent in axisymmetric Taylor-vortex flow. We have found numerically that the family of stable one-travelling-wave flows with differing $m_1$ and with the same values of $R$, $\lambda$ and $\eta$ have energy and enstrophy spectra with slopes $|\partial E/\partial k|$ and $|\partial \mathscr{E}/\partial k|$ that decrease with increasing $m_1$. The spectra in figure 21 which were calculated for $m_1 = 4$ and with the same values of $R$, $\lambda$ and $\eta$ as the $m_1 = 6$ flow in figure 14 have slopes that are greater than those in figure 14.

Figure 16, like figure 4, is a plot of the angular momentum per unit mass $L(r)$ as a function of radius. The broken curve is $L(r)$ for unstable circular Couette flow, the dotted curve for unstable axisymmetric Taylor-vortex flow, and the solid curve for stable non-axisymmetric one-travelling-wave flow. All three flows are computed with

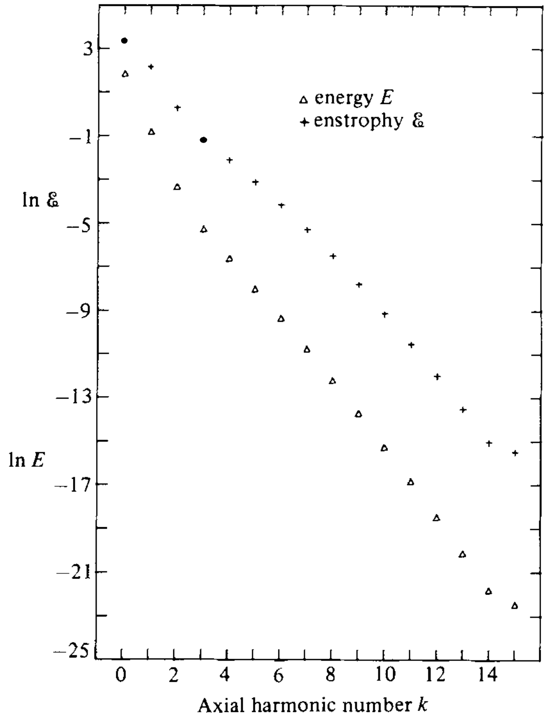

FIGURE 14. Energy and enstrophy spectra as functions of the axial harmonic number for the one-travelling-wave flow in figures 6 and 9.

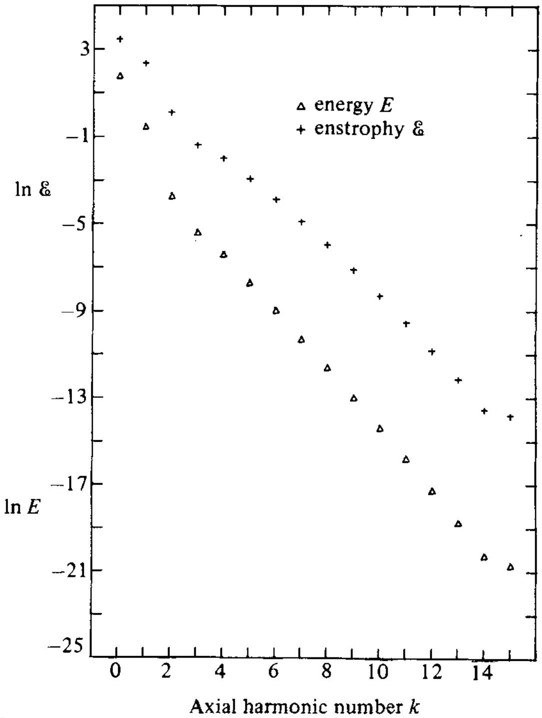

FIGURE 15. Energy and enstrophy spectra for the unstable Taylor-vortex flow computed with the same $R$, $\lambda$ and $\eta$ as figure 14.

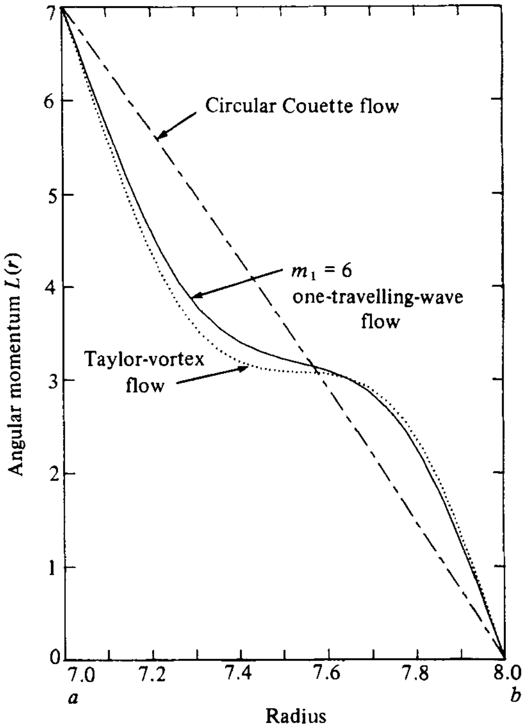

FIGURE 16. Angular momentum per unit mass $L(r)$ as a function of radius for three equilibrium flows, all with $R = 2.063R_c$, $\lambda = 3.00$ and $\eta = 0.875$: stable $m_1 = 6$, one-travelling-wave (solid curve), unstable Taylor-vortex (dotted curve), unstable circular Couette (dashed curve).

$R = 2.063R_c$, $\lambda = 3.00$ and $\eta = 0.875$. An interesting feature of figure 16 is that, far from the boundaries, the stable flow does not minimize the gradient of $L(r)$ or have the steepest gradient of $L(r)$ at the boundaries (i.e. greatest torque). Neither does the one-travelling-wave flow maximize the angular-momentum transport. This is in agreement with Davey *et al.* (1968), whose finite-amplitude calculations showed that the wavy-vortex flow has a smaller torque than that of the unstable axisymmetric Taylor-vortex flow. Figure 17 shows $L(r)$ for two flows with the same $R$, $\lambda$ and $\eta$ as in figure 16. The one-travelling-wave flows are represented by a solid curve for $m_1 = 4$ and a broken curve for $m_1 = 6$. Both flows are stable with respect to finite-amplitude perturbations in both the numerical and laboratory experiments, yet it is obvious that the $m_1 = 6$ flow is more efficient than the other in transporting angular momentum. In laboratory experiments the final equilibrium state that the fluid goes into depends on the initial conditions (i.e. how the apparatus is turned on and brought up to speed). Experimentalists (King & Swinney 1983) have found that, for the $R$, $\lambda$ and $\eta$ of the two flows in figure 17, a majority of initial conditions result in the $m_1 = 6$ flow being the final state.

### *The travelling mode as a secondary instability*

Because the torque of the travelling-wave flow is less than that of Taylor-vortex flow, it has been proposed that the travelling wave is a secondary instability of the Taylor-vortex flow and is not a centrifugal instability of the primary flow (cf. DiPrima & Swinney 1981). One picture that has been suggested for the secondary instability is that the shear in the $(\phi, z)$-plane has an Orr–Sommerfeld type of instability and

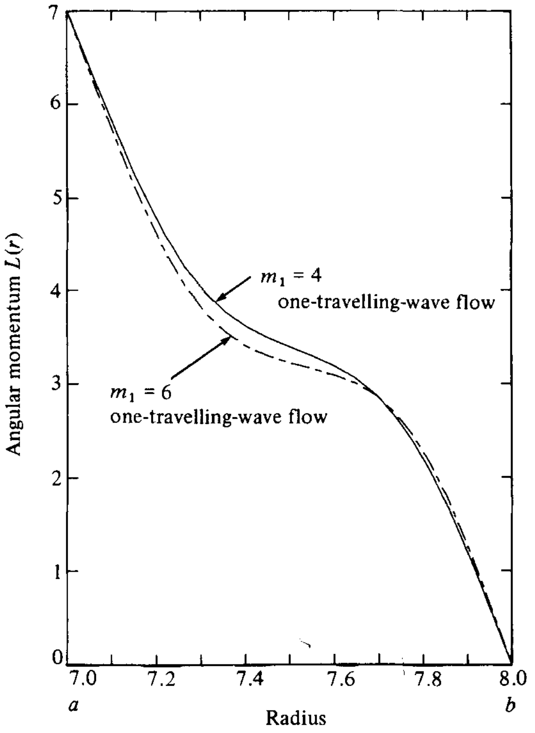

FIGURE 17. $L(r)$ for $m_1 = 6$ (dashed curve) and $m_1 = 4$ (solid curve), one-travelling-wave flows. Both flows are stable and have the same $R$, $\lambda$ and $\eta$ as the flow in figure 16.

that the travelling waves are associated with the inflection points of the shear, i.e. where $\partial^2 v_\phi/\partial z^2 = 0$ (Meyer 1966; Davey *et al.* 1968). Although this picture has several virtues, we propose another scenario for secondary instability which we believe has several advantages over the Orr–Sommerfeld picture.

First note that for $R = 2.063R_c$, $\lambda = 3.00$ and $\eta = 0.875$ the kinetic energy (per unit axial length) of the unstable Taylor-vortex flow is 6.2552, whereas the kinetic energy of the stable $m_1 = 6$ one-travelling-wave flow (with the same $R$, $\lambda$ and $\eta$) is 6.4524. The stable flow has slightly more total kinetic energy than the unstable flow. However, it is interesting to note that the kinetic energy in the radial direction is more than 10% greater for the *unstable* Taylor-vortex flow than for the *stable* one-travelling-wave flow. Furthermore, the $\phi$- and $z$-components of the kinetic energy are *lower* for the unstable Taylor-vortex flow. The radial energy in the one-travelling-wave flow is significantly lower than that of the Taylor-vortex flow because the velocity in the non-axisymmetric outflow boundary is diminished; the $\phi$- and $z$-components of the energy in the non-axisymmetric flow are greater than the corresponding components in Taylor-vortex flow owing to the presence of vortical motions in the $(z, \phi)$-plane (i.e. non-axisymmetric modes in figure 10). The axisymmetric component of the kinetic energy of the one-travelling-wave flow is 6.2360, which is less than the axisymmetric component of the kinetic energy (i.e. total energy) of Taylor-vortex flow (6.2552). The vortical motions in the $(z, \phi)$-plane associated with the one-travelling-wave flow have grown at the expense of the axisymmetric radial component of the kinetic energy in the outflow boundary of the Taylor-vortex flow.

The nonlinear travelling mode, whose $(r, z)$-projection is shown in figure 7, decreases the azimuthally averaged radial velocity in the outflow boundary. To show how this

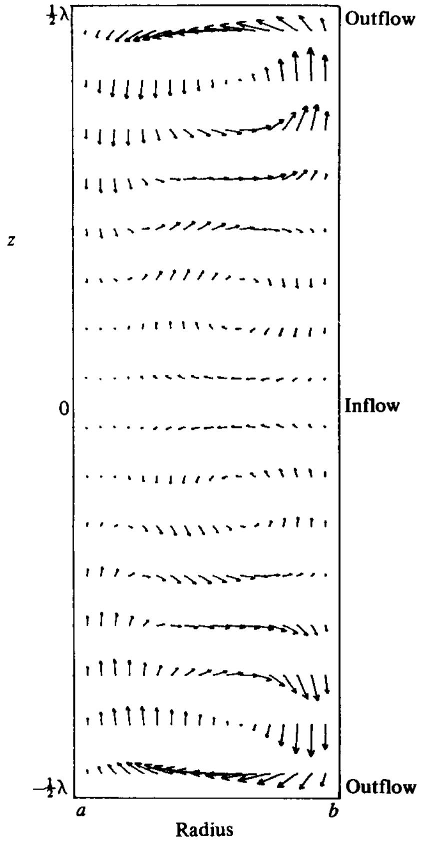

FIGURE 18. Axisymmetric component of the nonlinear travelling mode shown in figure 7. The nonlinear travelling mode decreases the radial velocity in the outflow boundary.

decrease comes about, we have computed the azimuthal average of the nonlinear travelling mode from figure 7 and plotted the $(r, z)$-projection in figure 18, which shows that the radial velocity of the nonlinear travelling mode is *inward* at $z = \pm\frac{1}{2}\lambda$, the location of the Taylor-vortex *outflow* boundary. Figure 18 also shows that the nonlinear travelling mode mixes the fluid at the centres of the Taylor vortices (figure 8), with the fluid near the cylinders' boundaries. At $z = 0$ the radial velocity of the nonlinear travelling mode is inward and slightly increases the radial velocity of the Taylor-vortex inflow boundary.

Based on the observation that the travelling-wave flow has converted part of its radial kinetic energy into azimuthal and axial kinetic energy, we believe that it is the radial jet in the outflow boundary that drives the one-travelling-wave instability. We view the transition to the one-travelling-wave flow as caused by a local, inviscid, centrifugal instability of the outflow boundary. Consider the Taylor-vortex flow shown in figure 2. Rayleigh's stability criterion states that a flow is centrifugally unstable whenever the angular momentum decreases outward from some reference point. At the inflow and outflow boundaries of the Taylor vortices, the $\phi$-component of the angular momentum with respect to the vortex centre decreases outward from the centre. The Taylor vortices themselves (as viewed in the $(r, z)$-plane) are centrifugally unstable. It is the nature of centrifugal instabilities to produce 3-dimensional secondary flows with vortical motion in the plane perpendicular to the primary flow. (The secondary Taylor-vortex flow driven by the centrifugally unstable circular Couette flow is the classic example.) Centrifugally unstable Taylor vortices (in the $(r, z)$-plane) produce a vortical secondary flow in the $(z, \phi)$-plane as in figure 10. The vortices in the $(z, \phi)$-plane not only break the axial symmetry of the Taylor-vortex flow (so the one-travelling-wave flow must be non-axisymmetric), but also, because they are centred near the outflow and inflow boundaries (i.e. $z \approx 0$ and $z \approx \pm\frac{1}{2}\lambda$), they mix fluid from the different Taylor vortices together at their inflow boundaries and thereby reduce the radial component of kinetic energy in the outflow boundary. We have found numerically that, at the critical Reynolds number where Taylor-vortex flow becomes unstable to one-travelling-wave flow, the vortices in the $(z, \phi)$-plane are centred exactly (to within numerical uncertainties) at the outflow and inflow boundaries at $z = 0$ and $z = \pm\frac{1}{2}\lambda$.

An Orr–Sommerfeld-type instability of the shear in the $(z, \phi)$-plane does not explain the fact that the radial kinetic energy of the one-travelling-wave flow is less than it is in the Taylor-vortex flow. Furthermore, if the travelling wave were a shear instability we would expect that the vortices in the $(z, \phi)$-plane would be centred at the inflection points. The inflection points of the azimuthal velocity in the $(z, \phi)$-plane (as well as the centres of the Taylor vortices) are located near $z = \pm\frac{1}{4}\lambda$ (the exact position is a function of radius). Figure 10 shows that the vortices are centred approximately 90° out of phase from the inflection points. We also note that a periodic array of vortices with alternating sign in the $(z, \phi)$-plane centred near the inflow and outflow boundaries (i.e. $z \approx 0$, $z \approx \pm\frac{1}{2}\lambda$, $z \approx \pm\lambda$, ...) is consistent with shift-and-reflect symmetry, whereas a periodic, alternating, array of vortices centred at the inflection points (i.e. $z \pm\frac{1}{4}\lambda$, $\pm\frac{3}{4}\lambda$, ...) is inconsistent.

Our picture that an instability of the radial outflow boundary is responsible for the one-travelling-wave flow dovetails nicely with our numerical findings (Marcus 1984*c*) that the second travelling wave is associated with an instability of the inflow boundary. Because the inflow jet is weaker than the outflow jet, the second travelling wave occurs at a higher Reynolds number. Therefore inflow/outflow instabilities provide a natural way for the Taylor–Couette flow to have both one- and two-travelling-wave instabilities with onset at different Reynolds numbers. (Having an inflectional instability produce both the one- and the two-travelling-wave flows is more difficult; since, although there are two inflection points per axial wavelength, the flow at the two points is identical and it is not obvious why one inflection point would go unstable at a low $R$ and the other at a high $R$.)

We have not been able to use our model of instability to predict the critical value of Reynolds number for onset of travelling waves as a function of radius ratio $\eta$. However, Coles (1965) did show experimentally that there is a relationship between the Reynolds number for the onset of wavy vortices and the characteristic angular velocity of the flow in the Taylor vortices (which is related to the velocity in the outflow jet). In the narrow-gap limit Davey *et al.* (1968) used the Orr–Sommerfeld shear instability to explain Coles' empirical determination of the critical Reynolds number as a function of $\eta$ (see Coles 1965, p. 401). Their explanation depends on the assumption that shear instability occurs when the local Reynolds number of the azimuthal velocity is approximately greater than 40. The Orr–Sommerfeld model does not explain how Taylor-vortex flow in wide-gap geometries, i.e. $\eta \approx \frac{1}{2}$, remains stable against non-axisymmetric modes even at very large Reynolds numbers. For wide-gap, stable, axisymmetric flows the local Reynolds number of the azimuthal velocity can exceed several thousand.

### *Wave speeds*

It is important to understand what determines the speed of the travelling waves, or equivalently the speed of the rotating frame in which the one-travelling-wave flow appears as a steady state. Figure 6 shows that the comoving surfaces, where the azimuthal velocity is the same as the speed of the travelling wave, pass near the centres of the Taylor vortices. The wave speed $s_1$ for $m_1 = 6$, $\lambda = 3.00$, $\eta = 0.875$ and $R = 2.063R_c$ is 0.05367 in dimensionless units, or 0.3757 times the angular velocity of the inner cylinder. In all of our computations with different values of $R$, $\lambda$, $m_1$ and $\eta$, the wave speed $s_1/\Omega_{in}$ is always less than unity. This means that the speed of the wave is always equal to the azimuthal velocity of fluid along some comoving surface.

To illustrate the importance of the comoving surface in Taylor–Couette flow, we have plotted in figure 19 the $(r, z)$-projection of the velocity of a neutrally stable, non-axisymmetric linear eigenmode of circular Couette flow with $\lambda = 2.968$ and $\eta = 0.868$ for three different values of $\phi$. This eigenmode is $m_1$ fold symmetric with $m_1 = 6$, and is a travelling wave with an azimuthal angular velocity of 0.07676 in dimensionless units, or 0.5048 times the inner cylinder speed. The comoving surfaces (solid curves) in figure 19 by definition pass through all fluid elements with the same angular velocity as the travelling eigenmode. The solid curves are straight lines because the eigenmode has an infinitesimal amplitude and the circular Couette velocity has no dependence on $z$ or $\phi$. For all values of $\phi$ the solid lines pass through the centres of the vortices to within the numerical accuracy of the calculation. *All non-axisymmetric eigenmodes of circular Couette flow that we have examined numerically have comoving surfaces that pass through the centres of their vortices.*

In the one-travelling-wave flow the comoving surfaces pass closer to the vortex centres (when viewed in the $(r, z)$-plane) as the Reynolds number decreases. In figure 20 we plot the $(r, z)$-projection of the velocity for $\eta = 0.875$, $\lambda = 2.50$, $m_1 = 6$ and for a Reynolds number just equal to the critical value where the $m_1 = 6$ travelling wave first becomes unstable, $R(m_1 = 6)_c$. The flow shown in figure 20 is the Taylor-vortex flow (plus a negligible contribution due to the very-small-amplitude $m_1 = 6$ travelling mode). The solid curve is the comoving surface and passes directly through the vortex centres. A $(z, \phi)$-projection of this flow shows that the comoving surfaces pass very close to, but not exactly through, the inflection points of the $(z, \phi)$-component of the velocity. In all flows for which we have calculated the critical Reynolds number for the onset of a travelling wave, we have found that the wave speed $s_1$ is equal to the azimuthal velocity of the fluid located at the centres of the Taylor vortices to within the numerical accuracy of the calculation. It is possible that the comoving surface and the vortex centres are offset by the thickness of a viscous sublayer. As the Reynolds number increases, the comoving surfaces move away from the vortex centres (see below). We note that the numerically calculated transition to the $m_1 = 6$ one-travelling-wave flow depicted in figure 20 cannot be reproduced in the laboratory at the Reynolds number at which the Taylor-vortex flow first becomes unstable to the $m_1 = 6$ travelling wave, since that wave is itself unstable to the $m_1 = 1$ travelling wave. Since in the laboratory the lowest Reynolds number at which the stable $m_1 = 6$ travelling wave can be measured is greater than $R(m_1 = 6)_c$, the observed wave always has finite amplitude and the comoving surfaces do not pass directly through the vortex centres.

For all Reynolds numbers that we have examined numerically, the comoving surfaces exist and $s_1/\Omega_{in}$ is less than unity. Because the wave speed near onset is approximately equal to the azimuthal angular velocity of the fluid at the vortex centres (which are geometrically constrained to be nearly midway between the inner and outer cylinders) and because, for $\eta \approx 0.875$, the angular velocity (in units of $\Omega_{in}$) midway between the cylinders varies between 0.3 and 0.5 (see figures 4, 16, 17, 22 and 23), the wave speeds $s_1/\Omega_{in}$ always lie between 0.3 and 0.5. As a result of this

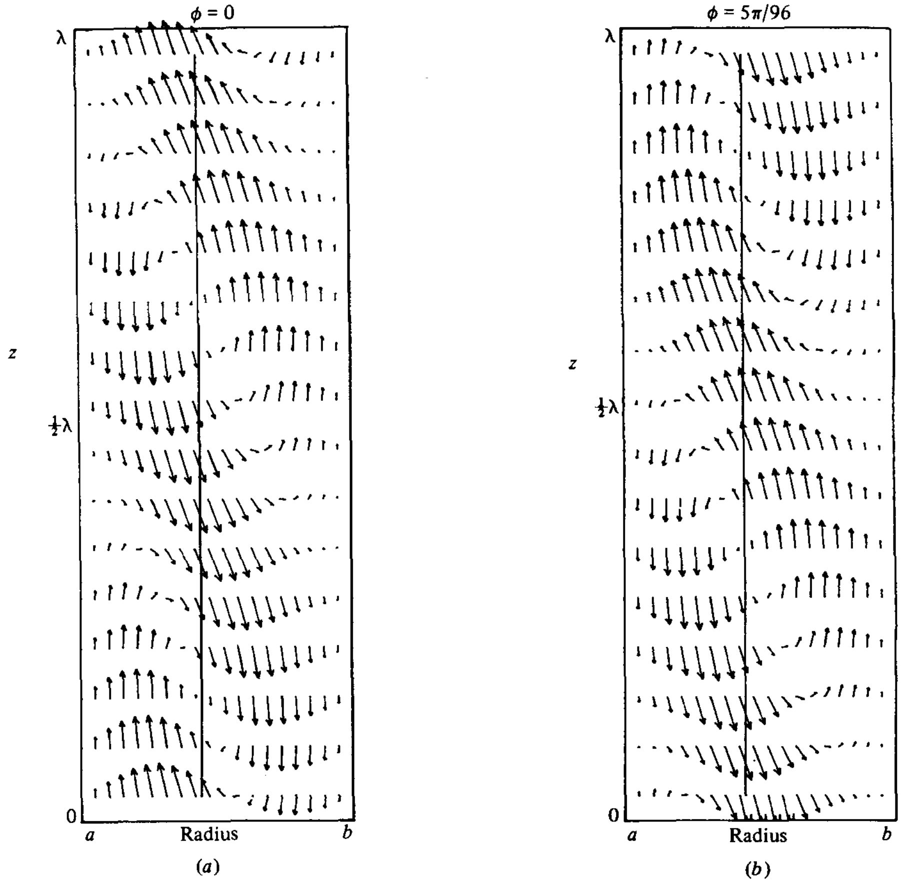

FIGURE 19(*a*, *b*). For caption see facing page.

constraint on the wave speed, even the poorest numerical computation with $\eta \approx 0.875$ will rarely miscalculate $s_1/\Omega_{\text{in}}$ by more than about 10% (see King *et al.* 1984).

There is one other piece of evidence that the nonlinear travelling mode is tied to a comoving surface of the fluid. In the Appendix of this paper and in King *et al.* (1984) marginal stability theory is used to compute the azimuthal velocity of Taylor–Couette flow for $R \gg R_c$ and $\eta \rightarrow 1$. In this limit the azimuthal angular velocity of the fluid not in the boundary layers is independent of the values of $\lambda$, $m_1$ (and $m_2$), and is approximately $0.5634\Omega_{\text{in}}$. If the travelling modes are tied to the comoving surfaces, if those surfaces are outside the boundary layers, and if the marginal stability theory is correct, then $s_1$ should also be equal to $0.5634\Omega_{\text{in}}$. The experimentally determined value of $s_1$ for $R \gg R_c$ (which has been extrapolated to $\eta = 1$ by fitting the data to a quartic polynomial) is equal to $0.563\Omega_{\text{in}}$ (King *et al.* 1984).

### *One-travelling-wave flow as a function of R*

For $R = 2.063R_c$, $\lambda = 3.00$ and $\eta = 0.875$ we have already seen that the kinetic energy $E(m_1 = 6)$ of $m_1 = 6$ one-travelling-wave flow obeys the relation $E(\text{CC}) > E(m_1 = 6) > E(\text{TV})$. However, at $\eta = 0.875$ both $E(m_1 = 6)/E(\text{CC})$ and $E(m_1 = 6)/E(\text{TV})$ decrease with increasing Reynolds number; for Reynolds numbers greater than about $2.75R_c$ we find $E(\text{CC}) > E(\text{TV}) > E(m_1 = 6)$. Since the main contribution to the kinetic energy is from $\hat{v}_\phi(r, m = 0, k = 0)$, it is not surprising that

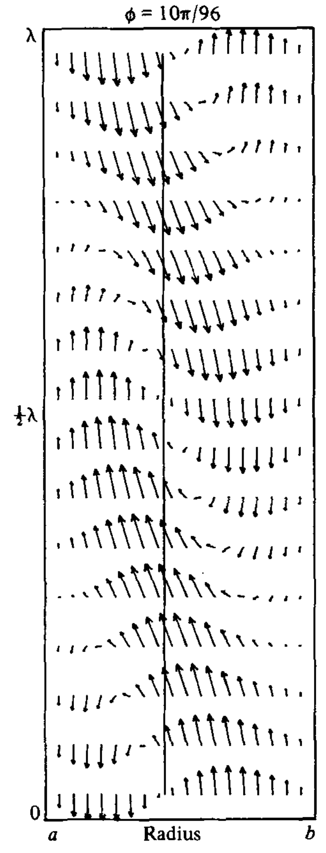

(*c*)

FIGURE 19. $(r, z)$-projection of an $m_1 = 6$ eigenmode of circular Couette flow with $R = 230.20$, $\lambda = 2.968$ and $\eta = 0.868$. The comoving surfaces (solid curves) pass through the centres of the Taylor vortices.

the angular momentum's dependence on $R$ is similar to the energy's dependence. For low values of $R$ (but high enough so the $m_1 = 6$ travelling mode is stable) we find that $\mathscr{L}(\mathrm{CC}) > \mathscr{L}(m_1 = 6) > \mathscr{L}(\mathrm{TV})$; for $R$ greater than approximately $2.75R_c$ we find that $\mathscr{L}(\mathrm{CC}) > \mathscr{L}(\mathrm{TV}) > \mathscr{L}(m_1 = 6)$. For all $R$ with $\eta = 0.875$ the angular-momentum timescale $\tau_{\mathscr{L}}$ is nearly equal to the dynamical timescale $\tau_p$.

In figures 16, 22 and 23 we show how the angular-momentum distribution $L(r)$ changes as the Reynolds number increases from $2.063R_c$ to $3.891R_c$. All three plots are for $m_1 = 6$ one-travelling-wave flows with $\lambda = 3.00$ and $\eta = 0.875$. The figures show that, as the Reynolds number becomes larger, the boundary layers become thinner, which causes $|\partial L/\partial r|$ in the interior of the flow to become smaller, and $|\partial L/\partial r|$ at the boundary to become larger. For Reynolds numbers greater than about $3.5R_c$ there are regions in the fluid where $\partial L(r)/\partial r$ is positive. The reversal of the angular-momentum gradient for large $R$ is analogous to the reversal of the mean temperature gradient in thermal convection for large Rayleigh numbers. The spatial region in which $\partial L(r)/\partial r$ is less than zero is similar to the convective overshoot region in thermal convection. In this overshoot region the local stability condition (Rayleigh's criterion for angular momentum and Schwarzschild's criterion for convection) states that the flow is stable.

We have already shown that $G$, $\dot{E}$ and $\mathscr{E}$ are closely coupled, and we have found

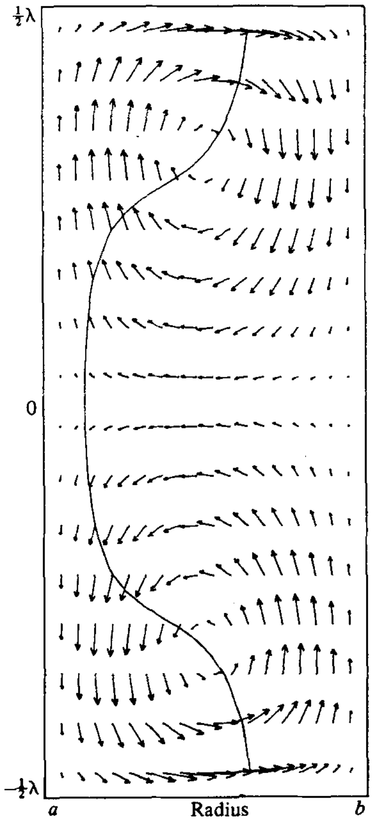

FIGURE 20. $(r, z)$-projection of the velocity for $\eta = 0.875$, $\lambda = 2.50$ and $m_1 = 6$ at the critical Reynolds number where the $m_1 = 6$ one-travelling-wave flow first becomes unstable. The comoving surface passes through the Taylor-vortex centres.

that the Reynolds-number dependence of these three quantities is similar. For the lowest values of $R$ at which the one-travelling-wave flows are stable, we find that

$$G(\mathrm{CC}) < G(m_1 = 6) < G(\mathrm{TV}), \quad \dot{E}(\mathrm{CC}) < \dot{E}(m_1 = 6) < \dot{E}(\mathrm{TV})$$

and

$$\mathscr{E}(\mathrm{CC}) < \mathscr{E}(m_1 = 6) < \mathscr{E}(\mathrm{TV});$$

but for $R/R_c > 3.5$ the flows have

$$G(\mathrm{CC}) < G(\mathrm{TV}) < G(m_1 = 6), \quad \dot{E}(\mathrm{CC}) < E(\mathrm{TV}) < \dot{E}(m_1 = 6)$$

and

$$\mathscr{E}(\mathrm{CC}) < \mathscr{E}(\mathrm{TV}) < \mathscr{E}(m_1 = 6).$$

The energy and enstrophy spectra as functions of the axial harmonic number for the $m_1 = 6$ one-travelling-wave flow with $R = 3.891R_c$, $\lambda = 3.00$ and $\eta = 0.875$ are plotted in figure 24. This plot shows that, with the exception of the smallest wavenumbers, $\ln E$ and $\ln \mathscr{E}$ are approximately linear in $k$. As $R$ increases, the slopes of the spectra decrease. The flow in figure 24 was computed with 32 axial Fourier modes. The insufficient axial resolution is clearly shown by the upward curl at $k = 15$. When the flow is recomputed with 64 axial modes the upward curl at $k = 15$ disappears, the points with $k < 15$ remain the same, and the spectra continue to be approximately linear in $k$ all the way to $k = 31$. The energy and enstrophy spectra

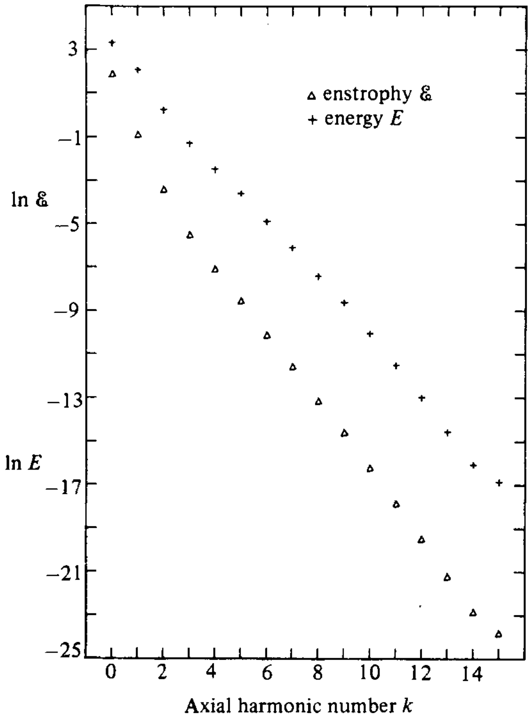

FIGURE 21. Energy and enstrophy spectra of the $m_1 = 4$ travelling-wave flow with the same $R$, $\lambda$ and $\eta$ as the flow in figure 14.

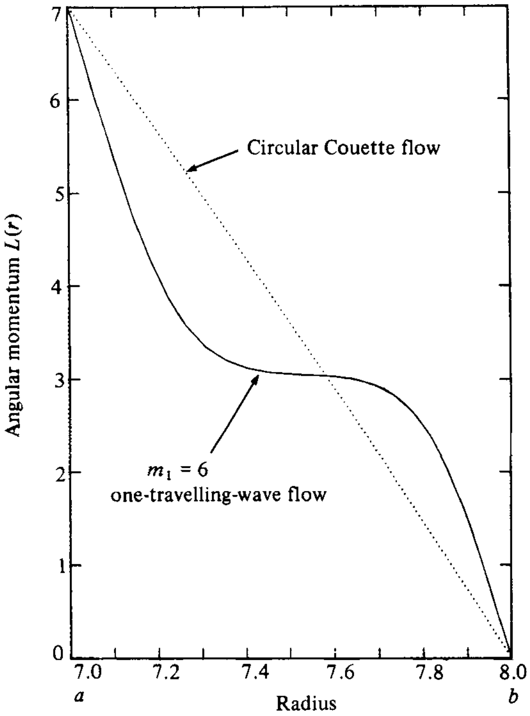

FIGURE 22. Angular momentum per unit mass $L(r)$ as a function of radius for the stable $m_1 = 6$ one-travelling-wave flow with $R = 2.948R_c$, $\lambda = 3.00$ and $\eta = 0.875$ (solid curve) and for the unstable Taylor-vortex flow with the same $R$, $\lambda$ and $\eta$ (dotted curve).

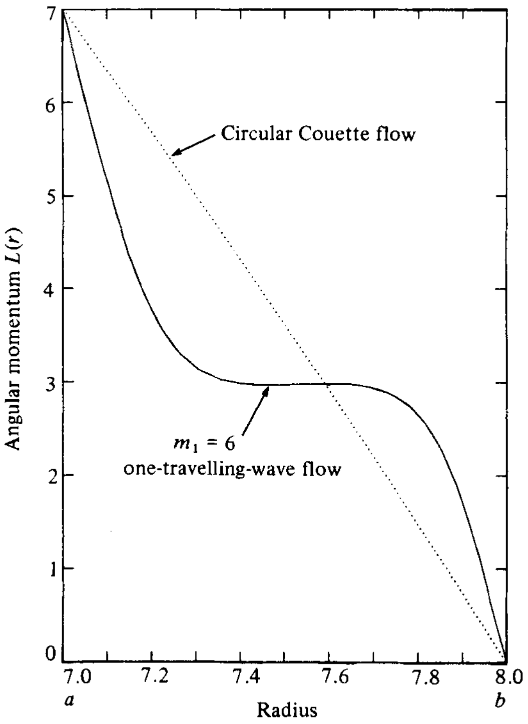

FIGURE 23. Same as figure 22 with $R = 3.96R_c$.

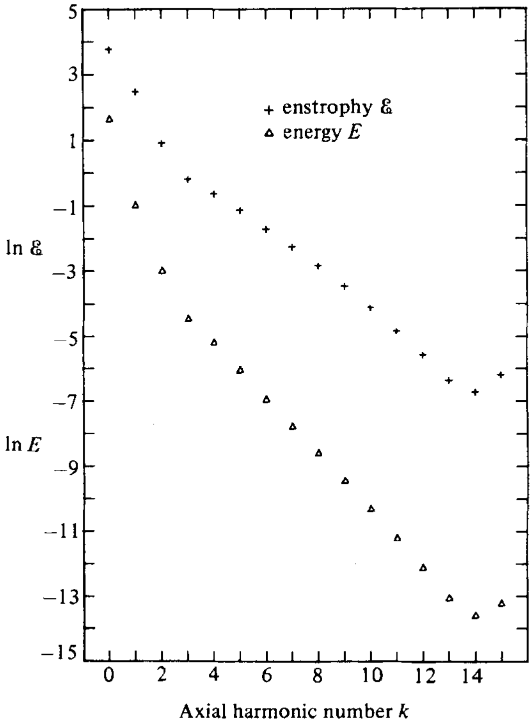

FIGURE 24. Energy and enstrophy spectra of the $m_1 = 6$ one-travelling-wave flow with $R = 3.981R_c$, $\lambda = 3.00$ and $\eta = 0.875$. The spectra are functions of axial harmonic number $k$.

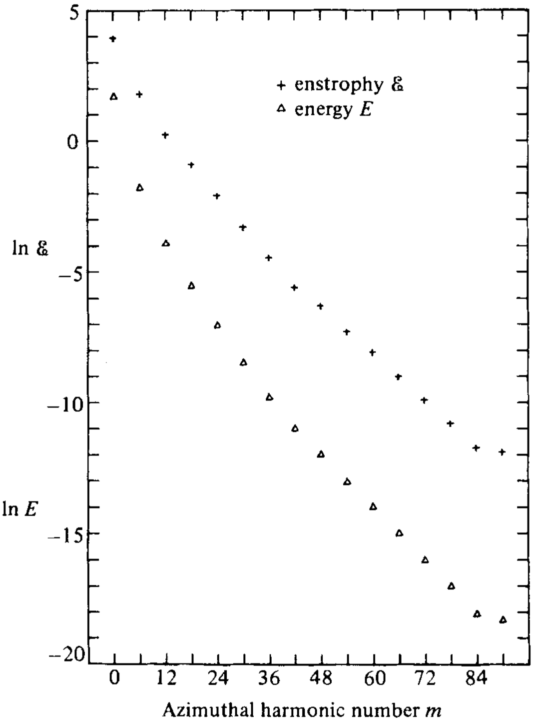

FIGURE 25. Energy and enstrophy spectra of the flow shown in figure 24 as functions of azimuthal wavenumber $m$. The energy $E(m)$ is the kinetic energy contained in all Fourier modes of the form $e^{im\phi}$.

for this same flow as functions of azimuthal harmonic number $m$ are shown in figure 25 (i.e. $E(m)$ is the energy contained in all Fourier modes of the form $\boldsymbol{v}(r,m,z)\,e^{\pm im\phi}$).

As the Reynolds number increases, the comoving surfaces where the fluid has angular azimuthal velocity $s_1$ move farther from the centres of the vortices. The 2-dimensional $(r,z)$-projection of the velocity field and the comoving surface (solid curve) for the $m_1 = 6$ one-travelling-wave flow with $R = 3.891R_c$, $\lambda = 3.00$ and $\eta = 0.875$ is shown in figure 26 (for an arbitrary value of $\phi$). The figure shows that, as the Reynolds number increases, the comoving surface moves away from the vortex centres. Figure 27 shows the nonlinear travelling mode of this flow for the same value of $\phi$ (i.e. the velocity in figure 26 minus the axisymmetric, unstable equilibrium Taylor-vortex velocity for the same $R$, $\lambda$ and $\eta$). The solid curve in figure 27 is the comoving surface in figure 26. We find that the nonlinear travelling mode has its maximum velocity at or near the comoving surface.

In order to show how the one-travelling-wave flow depends on $R/R_c$, we have listed the physical properties of the stable $m_1 = 6$ one-travelling-wave flows for $R/R_c = 2.0$, 3.891 and 5.97 in tables 3$(a,b,c)$. The three flows have nearly the same values of $\eta$ and $\lambda$ (see the table captions for the exact values). Each flow was calculated with 33 Chebyshev radial modes, and the sets of axial and azimuthal Fourier modes, $e^{im\phi}\,e^{i2\pi kz/\lambda}$, included in the calculations were such that $-M < m < M$ and $-K < k < K$. In tables 3$(a,b)$ $K = 16$. In table 3$(c)$ $K = 32$. In table 3$(a)$ $M = 48$, and in tables 3$(b,c)$ $M = 96$. In table 3 we have included $E$, $\mathscr{L}$, $G$ and $\dot{E}$, all of which are either dominated by or are exclusively due to the mean $(m = 0, k = 0)$ component of the azimuthal velocity. We have also listed several other quantities, such as the

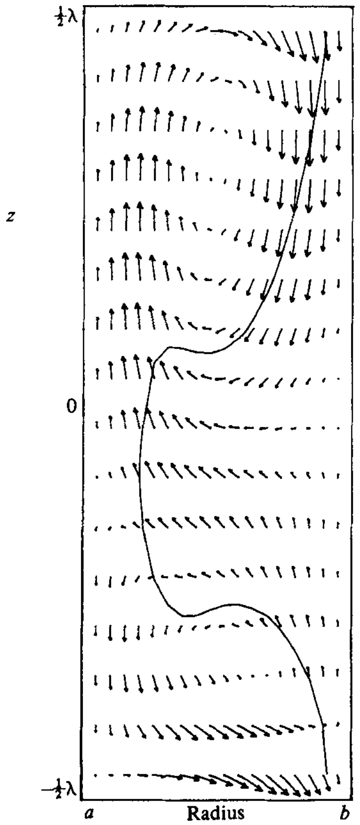

FIGURE 26. $(r, z)$-projection of the $m_1 = 6$ one-travelling-wave flow with $R = 3.891R_c$, $\lambda = 3.00$ and $\eta = 0.875$. For $R$ greater than the critical value for onset of the travelling wave, the comoving surface (solid curve) no longer passes through the vortex centres.

velocity correlation and the non-mean, or fluctuating, components of the energy, enstrophy, energy rate and r.m.s. velocity. These properties reflect the small-scale cellular motions of the fluid. Among the quantities included in table 3 are the fluctuating component of the kinetic energy

$$\tilde{E} \equiv E - \frac{1}{2}\int_a^b \mathrm{d}r\, r \int_0^{2\pi} \mathrm{d}\phi\, [\hat{\boldsymbol{v}}(r, k = 0, m = 0)]^2, \tag{4.1}$$

the fluctuating component of the enstrophy

$$\tilde{\mathscr{E}} \equiv \mathscr{E} - \frac{1}{2}\int_a^b \mathrm{d}r\, r \int_0^{2\pi} \mathrm{d}\phi\, [\boldsymbol{\nabla} \times \hat{\boldsymbol{v}}(r, k = 0, m = 0)]^2, \tag{4.2}$$

the fluctuating energy dissipation (or input) rate of the flow

$$\begin{aligned}\dot{\tilde{E}} &= -\frac{1}{\lambda}\int_0^\lambda \mathrm{d}z \int_0^{2\pi} \mathrm{d}\phi \int_a^b \mathrm{d}r\, r[\boldsymbol{v} - \hat{\boldsymbol{v}}(r, k = 0, m = 0)]\cdot[(\boldsymbol{v}\cdot\boldsymbol{\nabla})\,\boldsymbol{v}]\\ &= \frac{1}{\lambda}\int_0^\lambda \mathrm{d}z \int_0^{2\pi} \mathrm{d}\phi \int_a^b \mathrm{d}r\, r[\boldsymbol{v} - \hat{\boldsymbol{v}}(r, k = 0, m = 0)]\cdot\nabla^2\boldsymbol{v}\\ &= \frac{2}{R}\tilde{\mathscr{E}},\end{aligned} \tag{4.3}$$

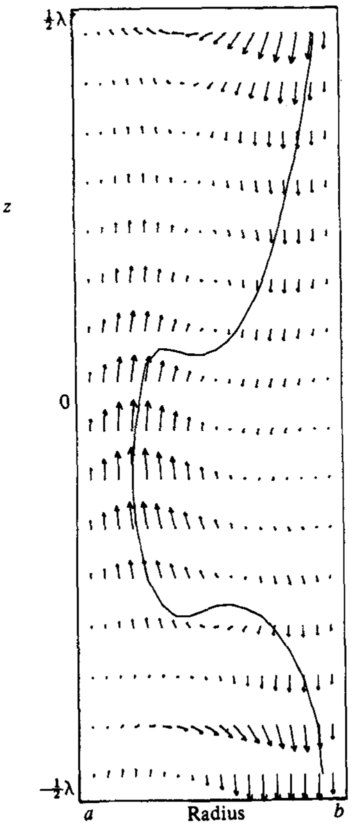

FIGURE 27. $(r, z)$-projection of the nonlinear travelling wave of the flow in figure 26 (i.e. the velocity in figure 26 minus the unstable Taylor-vortex velocity). The nonlinear travelling mode has its maximum amplitude at the comoving surface.

the timescale of the fluctuating energy

$$\tilde{\tau}_E \equiv \tilde{E}/\dot{\tilde{E}}, \tag{4.4}$$

the r.m.s. velocity fluctuations

$$\tilde{v}_{r\,\mathrm{rms}} \equiv \left[\int_0^\lambda \mathrm{d}z \int_0^{2\pi} \mathrm{d}\phi \int_a^b \mathrm{d}r\, r(v_r)^2 \Big/ \pi\lambda \frac{1+\eta}{1-\eta}\right]^{\frac{1}{2}}, \tag{4.5}$$

$$\tilde{v}_{z\,\mathrm{rms}} \equiv \left[\int_0^\lambda \mathrm{d}z \int_0^{2\pi} \mathrm{d}\phi \int_a^b \mathrm{d}r\, r(v_z)^2 \Big/ \pi\lambda \frac{1+\eta}{1-\eta}\right]^{\frac{1}{2}}, \tag{4.6}$$

$$\tilde{v}_{\phi\,\mathrm{rms}} \equiv \left[\int_0^\lambda \mathrm{d}z \int_0^{2\pi} \mathrm{d}\phi \int_a^b \mathrm{d}r\, r[v_\phi - \bar{v}_\phi(r, m=0, k=0)]^2 \Big/ \pi\lambda \frac{1+\eta}{1-\eta}\right]^{\frac{1}{2}}, \tag{4.7}$$

and the correlation between $\tilde{v}_r$ and $\tilde{v}_\phi$

$$C^2_{r,\phi} \equiv \frac{\displaystyle\int_0^\lambda \mathrm{d}z \int_0^{2\pi} \mathrm{d}\phi \int_a^b \mathrm{d}r\, r\, \tilde{v}_r \tilde{v}_\phi \Big/ \pi\lambda \frac{1+\eta}{1-\eta}}{\tilde{v}_{r\,\mathrm{rms}}\, \tilde{v}_{\phi\,\mathrm{rms}}}. \tag{4.8}$$

Each quantity in table 3 is expressed in three ways: in dimensionless units, in units of the same quantity calculated for circular Couette flow, and in units of the same

| | (a) | | | (b) | | | (c) | | |
|---|---|---|---|---|---|---|---|---|---|
| Quantity | Dimensionless units | Divided by value from circular Couette-flow | Divided by value from marginal-stability /mixing-length theory | Dimensionless units | Divided by value from circular Couette flow | Divided by value from marginal-stability /mixing-length theory | Dimensionless units | Divided by value from circular Couette flow | Divided by value from marginal-stability /mixing-length theory |
| $E$ | 6.1294 | 0.89195 | 0.81250 | 5.5673 | 0.76088 | 0.69886 | 4.8411 | 0.70448 | 0.64173 |
| $\mathscr{L}$ | 141.59 | 0.96863 | 0.69741 | 149.47 | 0.90625 | 0.66022 | 129.42 | 0.88538 | 0.63746 |
| $G$ | 2.7062 | 1.8589 | 2.8237 | 2.1545 | 2.6392 | 2.5852 | 1.6754 | 3.4354 | 2.5171 |
| $\dot{E}$ | 0.41155 | 1.8589 | 3.2531 | 0.30779 | 2.6392 | 2.9545 | 0.25479 | 3.4354 | 2.8999 |
| $\mathscr{E}$ | 41.184 | 2.1452 | 2.8353 | 64.744 | 3.1544 | 2.7103 | 81.774 | 4.2594 | 2.7156 |
| $\tau_E$ | 14.893 | 0.47981 | 0.25034 | 18.088 | 0.28830 | 0.23708 | 19.000 | 0.20506 | 0.22180 |
| $\tau_{\mathscr{L}}$ | 52.319 | 0.52106 | 0.24693 | 69.376 | 0.34338 | 0.25532 | 77.243 | 0.25772 | 0.25319 |
| $\tau_E/\tau_\nu$ | 0.064698 | 0.47981 | 0.25034 | 0.039343 | 0.28830 | 0.23708 | 0.027651 | 0.20506 | 0.22180 |
| $\tau_{\mathscr{L}}/\tau_\nu$ | 0.22728 | 0.52106 | 0.24693 | 0.15009 | 0.34338 | 0.25532 | 0.11241 | 0.25772 | 0.25319 |
| $\tau_E/\tau_\mathrm{p}$ | 0.36047 | 0.47981 | 0.25034 | 0.41126 | 0.28830 | 0.23708 | 0.45986 | 0.20506 | 0.22180 |
| $\tau_{\mathscr{L}}/\tau_\mathrm{p}$ | 1.2663 | 0.52106 | 0.24693 | 1.5774 | 0.34338 | 0.25532 | 1.8695 | 0.25772 | 0.25319 |
| $\tilde{E}$ | 0.43046 | — | 1.3384 | 0.45042 | — | 1.6233 | 0.41319 | — | 1.6381 |
| $\tilde{\mathscr{E}}$ | 12.286 | — | 5.6960 | 19.705 | — | 5.8657 | 26.215 | — | 5.8623 |
| $\tilde{\dot{E}}$ | 0.10675 | — | 5.6788 | 0.085719 | — | 5.8479 | 0.076302 | — | 5.8445 |
| $\tilde{\tau}_E$ | 4.0325 | — | 0.23569 | 5.2546 | — | 0.27758 | 5.4152 | — | 0.28028 |
| $\tilde{E}/E$ | 0.070229 | — | 1.6472 | 0.080904 | — | 2.3228 | 0.085351 | — | 2.5527 |
| $\tilde{\mathscr{E}}/\mathscr{E}$ | 0.29833 | — | 2.0090 | 0.30435 | — | 2.1642 | 0.32058 | — | 2.1588 |
| $\tilde{\dot{E}}/\dot{E}$ | 0.25938 | — | 1.7456 | 0.27850 | — | 1.9793 | 0.29947 | — | 2.0154 |
| $\tilde{\tau}_E/\tau_E$ | 0.27076 | — | 0.94148 | 0.29050 | — | 1.1171 | 0.28501 | — | 1.2637 |
| $\tilde{v}_{r\,\mathrm{rms}}$ | 0.037853 | — | 0.32558 | 0.046266 | — | 0.44027 | 0.054174 | — | 0.52617 |
| $\tilde{v}_{\phi\,\mathrm{rms}}$ | 0.11840 | — | 1.0183 | 0.10680 | — | 1.0163 | 0.10427 | — | 1.0127 |
| $\tilde{v}_{z\,\mathrm{rms}}$ | 0.062565 | — | 0.53813 | 0.074626 | — | 0.71014 | 0.069147 | — | 0.67158 |
| $\tilde{R}$ | 32.034 | — | 1.1992 | 63.566 | — | 1.3183 | 93.684 | — | 1.3268 |
| $C_{r,\phi}$ | 0.89283 | — | — | 0.72241 | — | — | 0.67334 | — | — |

TABLE 3. The physical properties of the $m_1 = 6$ one-travelling-wave flow with: (a) $R = 2.00R_\mathrm{c}$, $\eta = 0.868$, $\lambda = 2.14$, $R_\mathrm{c} = 115.1$; (b) $3.891R_\mathrm{c}$, 0.875, 2.32, 118.16; (c) $5.97R_\mathrm{c}$, 0.868, 2.20, 115.1. Quantities are given in (1) dimensionless units, (2) divided by the quantities from circular Couette flow with the same $\eta$ and $R$, and (3) divided by the quantities calculated with marginal-stability/mixing-length theory (valid in the limits $R \gg R_\mathrm{c}$ and $\eta \to 1$).

| Quantity from marginal-stability/mixing-length theory in limit $\eta \to 1$ | As functions of $1-\eta$ and $R/R_c$ | Divided by the same quantity for circular Couette flow |
|---|---|---|
| $E = \pi \int_a^b \mathrm{d}r\, r(L_0/r)^2$ | $0.996(1-\eta)^{-1}$ | $0.951$ |
| $\mathscr{E} = \frac{1}{2}R\dot{E} - 2\pi$ | $1.20(1-\eta)^{-1}(R/R_c)^{\frac{2}{3}}$ | $0.383(R/R_c)^{\frac{2}{3}}$ |
| $\mathscr{L} = 2\pi \int_a^b \mathrm{d}r\, rL_0$ | $3.54(1-\eta)^{-2}$ | $1.13$ |
| $G$ | $0.0581(1-\eta)^{-\frac{3}{2}}(R/R_c)^{-\frac{1}{3}}$ | $0.383(R/R_c)^{\frac{2}{3}}$ |
| $\dot{E}$ | $0.0581(1-\eta)^{-\frac{1}{2}}(R/R_c)^{-\frac{1}{3}}$ | $0.383(R/R_c)^{\frac{2}{3}}$ |
| $\tau_E = E/\dot{E}$ | $17.1(1-\eta)^{-\frac{1}{2}}(R/R_c)^{\frac{1}{3}}$ | $2.48(R/R_c)^{-\frac{2}{3}}$ |
| $\tau_{\mathscr{L}} = \mathscr{L}/G$ | $60.9(1-\eta)^{-\frac{1}{2}}(R/R_c)^{\frac{1}{3}}$ | $2.94(R/R_c)^{-\frac{2}{3}}$ |
| $L_0$ | $0.563(1-\eta)^{-1}$ | — |
| $\tau_E/\tau_\nu$ | $0.413(R/R_c)^{-\frac{2}{3}}$ | — |
| $\tau_{\mathscr{L}}/\tau_\nu$ | $1.47(R/R_c)^{-\frac{2}{3}}$ | — |
| $\tau_E/\tau_\mathrm{p}$ | $2.72(1-\eta)^{\frac{1}{2}}(R/R_c)^{\frac{1}{3}}$ | — |
| $\tau_{\mathscr{L}}/\tau_\mathrm{p}$ | $9.69(1-\eta)^{\frac{1}{2}}(R/R_c)^{\frac{1}{3}}$ | — |
| $\tilde{E} = \pi \int_a^b \mathrm{d}r\, r\tilde{v}_\mathrm{rms}^2$ | $0.376(R/R_c)^{-\frac{2}{9}}$ | — |
| $\tilde{\mathscr{E}} = \frac{1}{2}R\dot{\tilde{E}}$ | $1.35(R/R_c)^{\frac{2}{3}}$ | — |
| $\dot{\tilde{E}}$ | $0.0654(1-\eta)^{\frac{1}{2}}(R/R_c)^{-\frac{1}{3}}$ | — |
| $\tilde{\tau}_E = \tilde{E}/\dot{\tilde{E}}$ | $5.75(1-\eta)^{-\frac{1}{2}}(R/R_c)^{\frac{1}{9}}$ | — |
| $\tilde{E}/E$ | $0.378(1-\eta)(R/R_c)^{-\frac{2}{9}}$ | — |
| $\tilde{\mathscr{E}}/\mathscr{E}$ | $1.13(1-\eta)$ | — |
| $\dot{\tilde{E}}/\dot{E}$ | $1.13(1-\eta)$ | — |
| $\tilde{\tau}_E/\tau_E$ | $0.336(R/R_c)^{-\frac{2}{9}}$ | — |
| $\delta_\mathrm{in}$ | $1.14(R/R_c)^{-\frac{2}{3}}$ | — |
| $\delta_\mathrm{out}$ | $1.47(R/R_c)^{-\frac{2}{3}}$ | — |
| $\tilde{v}_\mathrm{rms}$ | $0.346(1-\eta)^{\frac{1}{2}}(R/R_c)^{-\frac{1}{9}}$ | — |
| $v_\nu$ | $0.210(1-\eta)^{\frac{1}{6}}(R/R_c)^{-\frac{1}{9}}$ | — |
| $\delta_\nu$ | $0.115(1-\eta)^{\frac{1}{3}}(R/R_c)^{-\frac{8}{9}}$ | — |
| $k_\mathrm{K}$ | $32.8(R/R_c)^{\frac{2}{3}}$ | — |
| $\tilde{v}(k_\mathrm{K})$ | $0.126(1-\eta)^{\frac{1}{2}}(R/R_c)^{-\frac{1}{3}}$ | — |
| $\tilde{v}(k_\mathrm{K})/\tilde{v}_\mathrm{rms}$ | $0.364(R/R_c)^{-\frac{2}{9}}$ | — |
| $\tilde{R} \equiv \tilde{v}_\mathrm{rms}\Omega_\mathrm{in}ad/\nu$ | $14.3(R/R_c)^{\frac{8}{9}}$ | — |

TABLE 4

quantity calculated from marginal stability and mixing-length theory. (In the third column of table 3, $\tilde{v}_{\phi\,\mathrm{rms}}$, $\tilde{v}_{r\,\mathrm{rms}}$ and $\tilde{v}_{z\,\mathrm{rms}}$ have all been normalized by $\tilde{v}_\mathrm{rms}$ from the mixing-length theory.) The marginal-stability/mixing-length theory is described in detail in the Appendix. The basic idea of the theory is to determine the characteristic r.m.s. velocity of the flow by assuming that $\tilde{\tau}_E \equiv \tilde{E}/\dot{\tilde{E}}$ is of the order of the turnaround time of the largest vortical motions and by requiring that the radial flux of angular momentum $F_L$ is equal to the torque. The theory is only valid in the limit $\eta \to 1$ and for $R \gg R_c$. The major results of the Appendix are summarized in table 4, where we list the physical quantities predicted by marginal-stability/mixing-length theory as functions of $R/R_c$ and $1-\eta$. The quantities are listed both in dimensionless units and in units of the same quantity calculated for circular Couette flow.

The flows in table 3 have values of $R/R_c$ that are not large and have values of $\eta$ not very close to unity. The fact that the last column of table 3 is not equal to unity indicates that the marginal-stability/mixing-length theory is not exact. Nonetheless, the Reynolds-number dependence predicted by the theory and summarized in table 4 is reflected accurately in the quantities listed in table 3: $\mathscr{E}$ and $\tilde{\mathscr{E}}$ increase approximately as $(R/R_c)^{\frac{2}{3}}$, $\tau_E$ and $\tau_{\mathscr{L}}$ increase approximately as $(R/R_c)^{\frac{1}{3}}$, and $G$, $\dot{E}$ and $\dot{\tilde{E}}$ decrease approximately as $(R/R_c)^{-\frac{1}{3}}$. Marginal-stability/mixing-length theory further predicts that $\mathscr{L}$, $E$, $\tilde{\mathscr{E}}/\mathscr{E}$, and $\tilde{E}/E$ are independent of $R/R_c$, and table 3 shows that the $(R/R_{\mathrm{c}})$-dependence of these quantities is weak. In fact, table 3 shows that $\mathscr{L}$ is non-monotonic in $R/R_{\mathrm{c}}$. The marginal-stability/mixing-length theory also predicts that $\tilde{v}_{\mathrm{rms}}$ and $\tilde{\tau}_E$ are proportional to $(R/R_{\mathrm{c}})^{-\frac{1}{9}}$ and $(R/R_{\mathrm{c}})^{\frac{1}{9}}$ respectively, and the numerical data in table 4 confirm that $\tilde{v}_{\mathrm{rms}}$ and $\tilde{\tau}_E$ are nearly independent of $R/R_{\mathrm{c}}$. The numerical values in table 3 show that $\tilde{E}$ is non-monotonic in $R/R_{\mathrm{c}}$, but decreases approximately as $(R/R_{\mathrm{c}})^{-\frac{2}{9}}$ as $R/R_{\mathrm{c}}$ varies from 3.891 to 5.97. This decrease is in accord with the marginal-stability/mixing-length theory. Table 3 also shows that the correlation $C_{r,\phi}$ decreases with increasing $R/R_{\mathrm{c}}$. One of the assumptions used in the Appendix to derive the mixing-length theory is that $C_{r,\phi}$ becomes small at $R \gg R_{\mathrm{c}}$.

It is important to remember that all of the stable one-travelling-wave flows with $\eta = 0.875$ occur at $R \lesssim 10R_{\mathrm{c}} \approx 1000$. Even though $R = 1000$ is often considered too large for accurate numerical simulation, the one-travelling-wave flow is very laminar at that value. More importantly from the point of view of a numericist, the range between the biggest and smallest lengthscales of the flow is not great. The reason why the flow is so laminar and the range of lengthscales is so small is that most of the kinetic energy of the flow is in the mean $(m = 0, k = 0)$ component of the azimuthal velocity, and there is very little energy in the fluctuations. The quantity that determines the range of lengthscales is the fluctuating Reynolds number $\tilde{R}$ based on $\tilde{v}_{\mathrm{rms}}$:

$$\tilde{R} \equiv \frac{v_{\mathrm{rms}}\,\Omega_{\mathrm{in}}\,ad}{\nu} = \tilde{v}_{\mathrm{rms}}R. \tag{4.9}$$

Table 3 shows that $\tilde{R} \approx 0.14R$ for one-travelling-wave flows with $\eta \approx 0.87$ and with $4 \lesssim R/R_{\mathrm{c}} \lesssim 6$. Marginal-stability/mixing-length theory predicts

$$\begin{aligned} \tilde{R} &\approx 14.3(R/R_{\mathrm{c}})^{\frac{8}{9}} \qquad (4.10)\\ &\approx 0.2R^{\frac{8}{9}} \quad \text{at} \quad \eta = 0.868. \end{aligned}$$

The maximum value of $R/R_{\mathrm{c}}$ for which the $m_1 = 6$ one-travelling-wave flow is stable is $R/R_{\mathrm{c}} \simeq 10$. For $R/R_{\mathrm{c}} = 10$, (4.10) gives $R \approx 110$. A flow with a Reynolds number of 110 is laminar, does not have a large range of lengthscales, and can be numerically simulated. The largest wavenumber of the fluctuating velocity field is the Kolmogoróv or dissipation wavenumber $k_{\mathrm{K}}$. It is estimated in the Appendix, and its value is listed in table 4. The ratio of the largest to the smallest lengthscale of the fluctuating velocity is $k_{\mathrm{K}}/2\pi$, and for $R/R_{\mathrm{c}} \approx 10$ it is approximately 24. With 33 radial, 32 axial and 32 azimuthal modes, a flow with a range of lengthscales equal to 24 should be well-resolved numerically.

The numerical results and the marginal-stability/mixing-length theory both show that $\dot{\tilde{E}}/\dot{E}$ is small, so most of the kinetic energy supplied by the motor driving the inner cylinder is dissipated by the mean $(m = 0, k = 0)$ azimuthal velocity in viscous sublayers. The characteristic velocity $v_\nu$ and thickness $\delta_\nu$ of the viscous sublayers are estimated in the Appendix, and are found to be

$$v_\nu = 0.210(1-\eta)^{\frac{1}{6}}(R/R_{\mathrm{c}})^{-\frac{1}{9}}, \tag{4.11}$$

$$\delta_\nu = 0.115(1-\eta)^{\frac{1}{3}}(R/R_{\mathrm{c}})^{-\frac{8}{9}}. \tag{4.12}$$

## 5. Discussion

In this paper we have presented detailed results of numerical simulations of wavy Taylor-vortex flow with one travelling wave. Rather than just reproduce the laboratory experiments, we have tried to use the numerics to gain insight into the underlying physics. Numerical simulations are similar to laboratory observations in that one rarely knows what to look for before one starts looking, and it is seldom that calculating one particular number or making one special measurement reveals something fundamental about the flow. Although numerical and laboratory experiments have some areas of overlap, such as the measurement of wave speeds, the two techniques really provide complementary information about Taylor–Couette flow. The strength of the computer simulation is that it determines details of the velocity and pressure everywhere, whereas the laboratory experiments can only measure the velocity at a few points. The strength of the experiments is that they allow an exploration of a wide range of $(R, \lambda, m_1, \eta)$-space, whereas repeated runs with different parameters on the computer are prohibitively expensive.

For each flow, the numerical simulations provide $3 \times 33 \times 32 \times 32$ pieces of information about the velocity. The most useful and least confusing ways of evaluating this abundance of data are plots of the 2-dimensional projections of the flow field and plots of the difference in velocity between two different equilibria. It has also been useful to compute energy and enstrophy spectra and the scalar quantities listed in table 4, which include the energy, angular momentum and dissipation rate.

We believe that numerical simulation is not an end in itself, but should provide the stimulus for developing simple physical models, back-of-the-envelope calculations and detailed analytic computations. This study has led us to postulate that the instability leading to one-travelling-wave flow is driven by the kinetic energy of the outflow boundary jet located between Taylor vortices. The travelling wave mixes together the fluid in the cores of neighbouring Taylor vortices and thereby creates non-axisymmetric vortical motions in the $(z, \phi)$-plane centred at the outflow and inflow boundaries.

Another result of this paper is that we have shown numerically that most of the kinetic energy is in the mean axisymmetric azimuthal velocity and very little cascades into the fluctuating component of the velocity. We have explained this result by using marginal stability theory and mixing-length theory and have shown that for large Reynolds number and for radius ratio $\eta$ near unity the fraction of energy that goes into the fluctuating component of the velocity is of order $1-\eta$. We have also shown numerically that the energy spectrum has the form $\ln E(k) \propto k^1$. Using a simple argument based on triad interactions, we have shown that for low Reynolds numbers this spectrum is derivable from the Navier–Stokes equation.

From the numerical simulations we have predicted the speeds of travelling waves: these results have been confirmed in the laboratory to within the accuracy of the experimental uncertainty (0.2 % fractional error). From the numerics we have developed the picture of the travelling wave being tied to a comoving surface within the fluid. This picture, along with marginal stability theory, predicts that at large Reynolds number and large radius ratio the wave speed should approach $0.563\Omega_{\text{in}}$. This prediction has also been confirmed in the laboratory to within the present experimental uncertainty (3 % fractional error). The numerics have shown that at the onset of the wavy vortices the wave speed of the travelling waves is equal to the azimuthal velocity of the fluid at the centres of the Taylor vortices. This relationship between the wave speed and the location of the Taylor vortices has been examined analytically by Bayly & Marcus (1983).

I thank G. King, S. Orszag, A. Patera and H. Swinney for useful discussions, and I thank A. Whittington for help in editing the manuscript. The numerical calculations were done on the CRAY-1 at the National Center for Atmospheric Research (operated by the National Science Foundation). This work was supported in part by NSF grants SPI-80-09181, MEA-82-15695 and ATM-80-17284 and by ONR-N00014-82-C-0451.

## Appendix. Marginal stability theory and mixing-length theory in the limits $R \gg R_c$, $\eta \to 1$

In King *et al.* (1984) an expression was derived for the torque $G$ of a Taylor–Couette flow using a marginal stability theory that was valid in the limits $R \gg R_c$ and $\eta \to 1$. This derivation was based on the observation that for $R \gg R_c$ the mean angular momentum $L(r) \equiv r\hat{v}_\phi(r,\ m=0,\ k=0)$ of a Taylor–Couette flow has a nearly constant value $L_0$ far from the boundaries, and has inner and outer boundary layers of thickness $\delta_{\text{in}}$ and $\delta_{\text{out}}$ respectively (cf. figure 22). The thicknesses of the boundary layers were determined by requiring that the *local* Taylor numbers of the boundary layers both be equal to the critical Taylor number that marks the onset of instability in circular Couette flow. The values of $G$, $L_0$, $\delta_{\text{in}}$ and $\delta_{\text{out}}$ determined by marginal stability theory are given in table 4 in dimensionless units as functions of $1-\eta$ and $R/R_c$. The torque derived from marginal stability theory is also given in units of $G$(CC) in table 4. Using the values of $G$ and $L_0$ we now derive approximations for the energy $E$, enstrophy $\mathscr{E}$, rate of energy input (or dissipation) $\dot{E}$, angular momentum $\mathscr{L}$, and the characteristic timescales for a Taylor–Couette flow in the limits $R \gg R_c$ and $\eta \to 1$.

The energy (per unit axial length) is primarily due to the $k=0$, $m=0$ mode (see below). Since $\hat{v}_r(r,\ m=0,\ k=0)$ and $\hat{v}_z(r,\ m=0,\ k=0)$ are identically equal to zero, we may approximate the energy by

$$\begin{aligned} E &\approx \frac{1}{2}\int_0^{2\pi} \mathrm{d}\phi \int_a^b \mathrm{d}r\, r[\hat{v}_\phi(r,\ m=0,\ k=0)]^2 \\ &\approx \pi \int_a^b \mathrm{d}r\, r(L_0/r)^2 \\ &= 0.996(1-\eta)^{-1}. \end{aligned} \tag{A 1}$$

The angular momentum (per unit axial length) can be approximated by

$$\mathscr{L} = \int_0^{2\pi} \mathrm{d}\phi \int_a^b \mathrm{d}r\, r\, L(r) \approx 2\pi \int_a^b \mathrm{d}r\, r\, L_0 = 3.54(1-\eta)^{-2}. \tag{A 2}$$

The rate of energy input is equal to $\Omega_{\text{in}} G$. Using the approximation for $G$ from table 4, we obtain

$$\dot{E} = 0.581(1-\eta)^{-\frac{1}{2}}(R/R_c)^{-\frac{1}{3}}. \tag{A 3}$$

In equilibrium the enstrophy is related to $E$ by (see §3)

$$\mathscr{E} = \tfrac{1}{2}R\dot{E} - 4\pi. \tag{A 4}$$

Using (A 3) with (A 4) we obtain

$$\mathscr{E} = 1.20(1-\eta)^{-1}(R/R_c)^{\frac{2}{3}}. \tag{A 5}$$

We can also obtain (A 5) by an alternative method. Our definition of enstrophy is

$$\mathscr{E} = \frac{1}{2}\int_0^{2\pi} \mathrm{d}\phi \int_a^b \mathrm{d}r\, r(\boldsymbol{\nabla} \times \boldsymbol{v})^2. \tag{A 6}$$

The main contribution to the vorticity in (A 6) is due to $\hat{v}_\phi(r, m=0, k=0)$. Far from the boundary layers where $L(r)$ is approximately constant, $\boldsymbol{\nabla} \times \hat{v}_\phi(r, m=0, k=0)\,\hat{\boldsymbol{e}}_\phi$ is equal to zero. In the outer boundary layer

$$|\boldsymbol{\nabla} \times \hat{v}_\phi(r, m=0, k=0)\,\hat{\boldsymbol{e}}_\phi| \approx \frac{L_0/b}{\delta_{\text{out}}}, \tag{A 7}$$

and in the inner boundary layer

$$|\boldsymbol{\nabla}\times\hat{\boldsymbol{v}}_\phi(r,m=0,k=0)\,\hat{\boldsymbol{e}}_\phi|\approx\frac{1-L_0/a}{\delta_{\mathrm{in}}}. \tag{A 8}$$

Using (A 7) and (A 8) with (A 6), we obtain

$$\begin{aligned}\mathscr{E}&\approx\pi\left[\int_a^{a+\delta_{\mathrm{in}}}\mathrm{d}r\,r\left(\frac{1-L_0/a}{\delta_{\mathrm{in}}}\right)^2+\int_{b-\delta_{\mathrm{out}}}^{b}\mathrm{d}r\,r\left(\frac{L_0/b}{\delta_{\mathrm{out}}}\right)^2\right.\\&=1.20(1-\eta)^{-1}\,(R/R_{\mathrm{c}})^{\frac{2}{3}}.\end{aligned} \tag{A 9}$$

Equation (A 9) is identical with (A 5).

Using (A 1)–(A 3), the energy timescale $\tau_E\equiv E/\dot{E}$ and angular momentum timescale $\tau_{\mathscr{L}}\equiv\mathscr{L}/G$ are

$$\tau_E=17.1(1-\eta)^{-\frac{1}{2}}\,(R/R_{\mathrm{c}})^{\frac{1}{3}} \tag{A 10}$$

and

$$\tau_{\mathscr{L}}=60.9(1-\eta)^{-\frac{1}{2}}\,(R/R_{\mathrm{c}})^{\frac{1}{3}}. \tag{A 11}$$

We now use mixing-length theory to derive an approximation for the r.m.s. radial and azimuthal velocities $\tilde{v}_{\mathrm{rms}}$ of the non-($k=0,m=0$) modes. We use the notation that a tilde above a quantity denotes the fluctuating part of the quantity, i.e. the part associated with all modes except the mean ($m=0,k=0$) mode. Using $\tilde{v}_{\mathrm{rms}}$, we will derive the kinetic energy $\tilde{E}$ of the fluctuating part of the flow, the enstrophy $\tilde{\mathscr{E}}$ of the fluctuations, the rate $\dot{\tilde{E}}$ at which energy enters (or is dissipated by the fluctuating part of the velocity, and the characteristic timescales of the fluctuating part of the flow. In particular we shall show that $\tilde{E}/E$ and $\dot{\tilde{E}}/\dot{E}$ are small.

For low-Reynolds-number flows ($R<4R_{\mathrm{c}}$) we can estimate $\tilde{v}_{\mathrm{rms}}$ by using the fact that in a steady state $2\pi r$ times the radial angular-momentum flux $F_L$ is independent of radius and is equal to $G$. Using (2.11) for $F_L$, we obtain

$$G=2\pi rF_L=\frac{r^3}{\lambda R}\int_0^{2\pi}\mathrm{d}\phi\int_0^{\lambda}\mathrm{d}z\frac{\partial(v_\phi/r)}{\partial r}+\frac{r^2}{\lambda}\int_0^{2\pi}\mathrm{d}\phi\int_0^{\lambda}\mathrm{d}z\,v_r\,v_\phi. \tag{A 12}$$

Far from boundaries, the viscous term (i.e. the term proportional to $R^{-1}$) on the right-hand side of (A 12) is negligible. Furthermore, for low values of $R$, the r.m.s. values of the fluctuating components of $v_r$ and $v_\phi$ are nearly equal and are well correlated (see §4 and table 3), so

$$\frac{1}{2\pi\lambda}\int_0^{2\pi}\mathrm{d}\phi\int_0^{\lambda}\mathrm{d}z\,v_r\,v_\phi\approx[\tilde{v}_{\mathrm{rms}}]^2. \tag{A 13}$$

Note that the mean ($k=0,m=0$) component of $v_\phi$ *never* contributes to the integral on the left-hand side of (A 13) because $v_r(r,m=0,k=0)\equiv0$. Using (A 13) in (A 12), ignoring the viscous term, and taking the limit $\eta\to1$, we obtain

$$\tilde{v}_{\mathrm{rms}}=(G/2\pi)^{\frac{1}{2}}\,(1-\eta)=0.0961(1-\eta)^{\frac{1}{4}}\,(R/R_{\mathrm{c}})^{\frac{1}{6}}. \tag{A 14}$$

For larger values of the Reynolds number we cannot use (A 13) and (A 14) because, as the flow becomes more complicated, $v_r$ and $v_\phi$ become poorly correlated:

$$\frac{1}{2\pi\lambda}\int_0^{\lambda}\mathrm{d}\phi\int_0^{\lambda}\mathrm{d}z\,v_r\,v_\phi\ll[\tilde{v}_{\mathrm{rms}}]^2. \tag{A 15}$$

To estimate $\tilde{v}_{\mathrm{rms}}$ in a complicated flow, we use an energy-balance argument, so it is necessary first to find an expression for $\dot{\tilde{E}}$. The energy that goes into the fluctuating velocity is supplied from the small but non-zero gradient of the mean angular momentum $L(r)$. We assume that far from the boundaries $L(r)$ is of the form

$$L(r) = L_0 - \Delta L\left(r - \frac{1}{1-\eta}\right), \tag{A 16}$$

where $\Delta L$ is a positive constant that provides a small correction to the relationship $L(r) = L_0$. Consider the adiabatic exchange of two fluid elements of equal volume located at $r$ and $r + \Delta r$ such that each element conserves its axial component of angular momentum. The energy liberated per unit volume from the mean azimuthal velocity in the exchange is

$$\Delta\tilde{E} = [L(r+\Delta r)^2 - L(r)^2]\left[\frac{1}{(r+\Delta r)^2} - \frac{1}{r^2}\right]. \tag{A 17}$$

Identifying $\Delta r$ as a mixing-length and setting it equal to unity, we obtain

$$\Delta\tilde{E} = 4L\,\Delta L(1-\eta)^3. \tag{A 18}$$

Rayleigh's inviscid stability condition is of course contained in (A 18). Using the facts that the energy $\Delta\tilde{E}$ is supplied to the fluctuating velocity once per eddy turnaround time $2/\tilde{v}_{\mathrm{rms}}$ and that the volume of fluid per unit axial length is $2\pi(1-\eta)^{-1}$, we obtain the rate (per unit axial length) at which energy is supplied to the fluctuating velocity in the limit $\eta \rightarrow 1$:

$$\dot{\tilde{E}} = 4L_0\,\Delta L\tilde{v}_{\mathrm{rms}}(1-\eta)^2. \tag{A 19}$$

The final relationship that we need before determining $\dot{\tilde{E}}$ is one between $\Delta L$ and the angular-momentum flux or torque. The radial angular-momentum flux $F_L$ is approximately equal to the product of the r.m.s. radial velocity and the mean angular-momentum excess $\Delta L$:

$$\frac{G}{2\pi r} = F_L = \tilde{v}_{\mathrm{rms}}\,\Delta L. \tag{A 20}$$

Equations (A 3), (A 19) and (A 20) along with the expressions for $L_0$ and $G$ in table 4 combine to give

$$\dot{\tilde{E}} = 1.13(1-\eta)\,\dot{E} = 0.0654(1-\eta)^{\frac{1}{2}}\,(R/R_{\mathrm{c}})^{-\frac{1}{3}}. \tag{A 21}$$

Notice that (A 21) shows that the ratio $\dot{\tilde{E}}/\dot{E}$ is very small.

A more rigorous but less physical way to derive (A 21) is to use the Navier–Stokes equation directly to obtain the energy input rate into the fluctuating velocity field. From (3.9) we see that $\dot{\tilde{E}}$ is due to nonlinear interactions and is exactly equal to

$$\dot{\tilde{E}} = -\frac{1}{\lambda}\int_0^\lambda \mathrm{d}z \int_0^{2\pi} \mathrm{d}\phi \int_a^b \mathrm{d}r\, r[\boldsymbol{v} - \hat{\boldsymbol{v}}_\phi(r, m=0, k=0)\,\hat{\boldsymbol{e}}_\phi]\cdot[(\boldsymbol{v}\cdot\boldsymbol{\nabla})\,\boldsymbol{v}]. \tag{A 22}$$

After integration by parts, (A 22) becomes

$$\dot{\tilde{E}} = -\frac{1}{\lambda}\int_a^b \mathrm{d}r \frac{\partial}{\partial r}\left[\frac{\hat{\boldsymbol{v}}_\phi(r, m=0,\ k=0)}{r}\right]\int_0^\lambda \mathrm{d}z \int_0^{2\pi} \mathrm{d}\phi\, r^2 v_r v_\phi. \tag{A 23}$$

Recognizing the fact that $(1/\lambda)\int_0^\lambda \mathrm{d}z \int_0^{2\pi} \mathrm{d}\phi\, v_r v_\phi$ is negligible in the boundary layers and that far from the boundaries (A 12) is applicable, (A 23) becomes

$$\dot{\tilde{E}} = -G\int_a^b \mathrm{d}r \frac{\partial}{\partial r}\left[\frac{L(r)}{r^2}\right], \tag{A 24}$$

where we have used $\hat{v}_\phi(r, m=0, k=0) = L(r)/r$. Substituting the expression for $L(r)$ from (A 16) into equation (A 24), we immediately obtain (A 21).

The rate at which energy enters the fluctuating velocity is balanced by the dissipation rate from the fluctuations. If we assume that the largest eddies lose all of their energy in one turnaround time, then

$$\dot{\tilde{E}} = \tfrac{1}{2}\pi(1-\eta)^{-1}\,\tilde{v}^3_{\mathrm{rms}}, \tag{A 25}$$

where we have used $2/\tilde{v}_{\mathrm{rms}}$ as the eddy turnaround time. (We have found numerically that (A 25) is approximately true even at Reynolds numbers as low as $5R_{\mathrm{c}}$.) Comparing (A 21) with (A 25), we obtain

$$\tilde{v}_{\mathrm{rms}} = 0.346(1-\eta)^{\frac{1}{2}}\,(R/R_{\mathrm{c}})^{-\frac{1}{9}}. \tag{A 26}$$

Using this value of $\tilde{v}_{\mathrm{rms}}$ in (A 19) along with (A 16) and (A 18) gives

$$\Delta\tilde{E} = \tfrac{1}{2}\tilde{v}^2_{\mathrm{rms}} = 0.0600(1-\eta)\,(R/R_{\mathrm{c}})^{-\frac{2}{9}}, \tag{A 27}$$

$$\frac{\Delta L}{L_0} = 0.0473(R/R_{\mathrm{c}})^{-\frac{2}{9}},$$

$$\frac{\partial L(r)}{\partial r} = 0.0266(1-\eta)^{-1}\,(R/R_{\mathrm{c}})^{-\frac{2}{9}}. \tag{A 28}$$

The kinetic energy $\tilde{E}$ of the fluctuating part of the velocity field is defined in terms of $\tilde{v}_{\mathrm{rms}}$ by

$$\tilde{E} \equiv \frac{1}{2}\int_0^{2\pi} \mathrm{d}\phi\,\mathrm{d}r\, r\tilde{v}^2_{\mathrm{rms}}, \tag{A 29}$$

and is equal to

$$\tilde{E} = 0.376(R/R_{\mathrm{c}})^{-\frac{2}{9}}. \tag{A 30}$$

The enstrophy associated with the fluctuating velocity is determined by using the fact that in equilibrium (see (3.9))

$$\tilde{\mathscr{E}} = \tfrac{1}{2}R\dot{\tilde{E}} = 1.35(R/R_{\mathrm{c}})^{\frac{2}{3}}. \tag{A 31}$$

The ratios $\tilde{E}/E$ and $\tilde{\mathscr{E}}/\mathscr{E}$ are both small:

$$\tilde{E}/E = 0.378(1-\eta)\,(R/R_{\mathrm{c}})^{-\frac{2}{9}}, \tag{A 32}$$

$$\tilde{\mathscr{E}}/\mathscr{E} = 1.13(1-\eta). \tag{A 33}$$

Equations (A 32) and (A 33) along with (A 21) confirm that the fluctuation velocity is energetically insignificant compared to the mean azimuthal velocity. We define the timescale that is characteristic of the kinetic energy of the fluctuating velocity field as

$$\tilde{\tau}_E = \tilde{E}/\dot{\tilde{E}} = 5.75(1-\eta)^{-\frac{1}{2}}\,(R/R_{\mathrm{c}})^{\frac{1}{9}}. \tag{A 34}$$

This timescale is less than but almost equal to $\tau_E$:

$$\tilde{\tau}_E/\tau_E = 0.336(R/R_{\mathrm{c}})^{-\frac{2}{9}}. \tag{A 35}$$

In making contact between turbulent Taylor–Couette flow and the classical theories of turbulence, it appears that the Reynolds number $R$, the energy $E$ and the energy input rate $\dot{E}$ should not be used since most of the energy of the flow is not in the fluctuations; instead the fluctuating quantities $\tilde{E}$ and $\dot{\tilde{E}}$ should be used. The Reynolds number associated with the fluctuating velocity field is defined as

$$\tilde{R} \equiv \tilde{v}_{\mathrm{rms}}\frac{\mathrm{d}a\Omega_{\mathrm{in}}}{\nu} = 14.3(R/R_{\mathrm{c}})^{\frac{5}{9}}. \tag{A 36}$$

Using the *fluctuating* quantities, we compute a Kolmogorov wavenumber $\tilde{k}_K$ and velocity $\tilde{v}(\tilde{k}_K)$. The 'Reynolds number' constructed from $\tilde{v}(\tilde{k}_K)$, $\tilde{k}_K$ and $\nu$ is by definition equal to unity, or in dimensionless units

$$\frac{2\pi\tilde{v}(\tilde{k}_K)}{\tilde{k}_K} = R^{-1} \tag{A 37}$$

The viscous dissipation of kinetic energy of the fluctuating component of the velocity is dominated by the dissipation at the Kolmogorov lengthscale, or

$$\dot{\tilde{E}} \approx \frac{1}{\lambda R}\int_0^{2\pi} \mathrm{d}\phi \int_0^{\lambda} \mathrm{d}z \int_a^b \mathrm{d}r\, r(\tilde{v}(\tilde{k}_K)\,\tilde{k}_K)^2,$$

$$\dot{\tilde{E}} \approx \frac{2\pi}{\lambda R}(1-\eta)^{-1}\,(\tilde{v}(\tilde{k}_K)\,\tilde{k}_K)^2. \tag{A 38}$$

Using (A 37) and (A 38) with (A 21), we obtain

$$\tilde{v}(\tilde{k}_K) = 0.126(1-\eta)^{\frac{1}{2}}\,(R/R_c)^{-\frac{1}{3}}, \tag{A 39}$$

$$\tilde{k}_K = 32.8(R/R_c)^{\frac{2}{3}}. \tag{A 40}$$

Note that (A 26) and (A 39) show that the ratio of the velocity of the smallest eddy to the velocity of the largest eddy is

$$\frac{\tilde{v}(\tilde{k}_K)}{\tilde{v}_{\mathrm{rms}}} = 0.364\left(\frac{R}{R_c}\right)^{-\frac{2}{9}}. \tag{A 41}$$

Equation (A 41) shows that

$$\frac{\tilde{v}(\tilde{k}_K)}{\tilde{v}_{\mathrm{rms}}} \propto (\tilde{k}_K)^{-\frac{1}{3}}. \tag{A 42}$$

The exponent of $-\frac{1}{3}$ in (A 42) is consistent with the Kolmogorov prediction that the velocity at wavenumber $k$ be proportional to $k^{-\frac{1}{3}}$ (or equivalently that the kinetic-energy spectrum has a $\frac{5}{3}$-power law. The use of (A 25), (A 37) and (A 38) alone (and no other assumptions of this Appendix) lead to (A 42).

In our picture of Taylor–Couette flow most of the mean kinetic energy in the $\hat{v}_{\phi}(r, m = 0, k = 0)$ mode is directly dissipated by that mode and does not cascade into $\tilde{E}$. We assume that the mean kinetic energy is dissipated in viscous sublayers at the inner and outer cylinders at a rate approximately equal to $\dot{E}$. We now estimate the characteristic thickness $\delta_\nu$ and velocity $v_\nu$ of the sublayers. We assume that the viscous sublayers have local Reynolds numbers of order unity, or

$$\delta_\nu v_\nu = R^{-1}. \tag{A 43}$$

The dissipation of the mean kinetic energy in the fluid is due to the dissipation in the sublayers. Therefore the dissipation rate is equal to $-R\boldsymbol{v}\cdot\nabla^2\boldsymbol{v}$, integrated over the volume of the sublayers (not the entire volume of the fluid). The volume (per unit axial length) of the sublayer is approximately $2\pi(1-\eta)^{-1}\,\delta_\nu$, so

$$\dot{E} \approx \frac{2\pi(1-\eta)^{-1}}{R}\delta_\nu\frac{v_\nu^2}{\delta_\nu^2}. \tag{A 44}$$

Equations (A 43) and (A 44) combine to give

$$v_\nu = 0.210(1-\eta)^{\frac{1}{6}}\,(R/R_c)^{-\frac{1}{9}}, \tag{A 45}$$

$$\delta_\nu = 0.115(1-\eta)^{\frac{1}{3}}\,(R/R_c)^{-\frac{8}{9}}. \tag{A 46}$$

## REFERENCES

ANDERECK, D. C., DICKMAN, R. & SWINNEY, H. L. 1983 New flows in a circular Couette system with co-rotating cylinders. *Phys. Fluids* **26**, 1395.

BAYLY, B. J. & MARCUS, P. S. 1983 Analytic calculation of Taylor–Couette wavespeeds. *Bull. Am. Phys. Soc.* **28**, 1397.

CHANDRASEKHAR, S. 1961 *Hydrodynamic and Hydromagnetic Stability.* Oxford University Press.

COLES, D. 1965 Transition in circular Couette flow. *J. Fluid Mech.* **21**, 385.

DAVEY, A. 1962 The growth of Taylor vortices in flow between rotating cylinders. *J. Fluid Mech.* **14**, 336.

DAVEY, A., DIPRIMA, R. C. & STUART, J. T. 1968 On the instability of Taylor vortices. *J. Fluid Mech.* **31**, 17.

DIPRIMA, R. C. & SWINNEY, H. L. 1981 Instabilities and transition in flow between concentric rotating cylinders. In *Hydrodynamic Instabilities and the Transition to Turbulence* (ed. H. L. Swinney & J. P. Gollub), p. 139. Springer.

EAGLES, P. M. 1971 On the stability of Taylor vortices by fifth-order expansions. *J. Fluid Mech.* **49**, 529.

JONES, C. A. 1981 Nonlinear Taylor vortices and their stability. *J. Fluid Mech.* **102**, 253–265.

KING, G. P. 1983 Limits of stability and irregular flow patterns in wavy vortex flow. Ph.D. thesis, University of Texas.

KING, G. P., LI, Y., LEE, W., SWINNEY, H. L. & MARCUS, P. S. 1984 Wave speeds in wavy Taylor-vortex flow. *J. Fluid Mech.* **141**, 365–390.

KING, G. P. & SWINNEY, H. L. 1983 Limits of stability and irregular flow patterns in wavy vortex flow. *Phys. Rev.* A **27**, 1240.

MARCUS, P. S. 1980 Stellar convection. II. A multi-mode numerical solution for convection in spheres. *Astrophys. J.* **239**, 622.

MARCUS, P. S. 1984*a* Simulation of Taylor–Couette flow. Part 1. Numerical methods and comparison with experiment. *J. Fluid Mech.* **146**, 45–64.

MARCUS, P. S. 1984*b* Simulation of Taylor–Couette flows with corotating cylinders. (To be submitted to *J. Fluid Mech.*)

MARCUS, P. S. 1984*c* Simulation of modulated wavy vortex flow in a Taylor–Couette system. (To be submitted to *J. Fluid Mech.*)

MEYER, K. A. 1966 *Los Alamos Rep.* LA-3497.

MEYER, K. A. 1969*a* *Los Alamos Rep.* LA-4202.

MEYER, K. A. 1969*b* Three-dimensional study of flows between concentric rotating cylinders. *Phys. Fluids Suppl.* **12**, II-165.

MEYER-SPASCHE, R. & KELLER, H. B. 1980 Computations of the axisymmetric flow between rotating cylinders. *J. Comp. Phys.* **35**, 100.

MOSER, R. D., MOIN, P. & LEONARD, A. 1983 A spectral numerical method for the Navier–Stokes equation with applications to Taylor–Couette flow. *J. Comp. Phys.* **52**, 524.

RAYLEIGH, LORD 1920 On the stability of the laminar motion of an inviscid fluid. In *Scientific Papers*, vol. VI, p. 197. Cambridge University Press.

RICHTMYER, R. D. 1981 A method for the calculation of invariant manifolds in hydrodynamic stability problems. *NCAR Tech. Note* TN-176+STR.

SHAW, R. S., ANDERECK, C. D., REITH, L. A. & SWINNEY, H. L. 1982 Superposition of traveling waves in the circular Couette system. *Phys. Rev. Lett.* **48**, 1172.

STUART, J. T. 1958 On the non-linear mechanics of hydrodynamic stability. *J. Fluid Mech.* **4**, 1.

YAHATA, H. 1983 Temporal development of the Taylor vortices in a rotating fluid, V. *Prog. Theor. Phys.* **69**, 396.

ZHANG, L. H. & SWINNEY, H. L. 1984 Wavy modes in turbulent Taylor-vortex flow. (To be submitted to *J. Fluid Mech.*)